

**Effect of Microstructure on the Static and Dynamic  
Behavior of Recycled Asphalt Material**

**Martin H. Sadd, Arun Shukla,  
Venkitanarayanan Parameswaran, and Qingli Dai  
University of Rhode Island**

**July 2002**

**URITC PROJECT NO. 536138**

**PREPARED FOR**

**UNIVERSITY OF RHODE ISLAND  
TRANSPORTATION CENTER**

**DISCLAIMER**

This report, prepared in cooperation with the University of Rhode Island Transportation Center, does not constitute a standard, specification, or regulation. The contents of this report reflect the views of the author(s) who is (are) responsible for the facts and the accuracy of the data presented herein. This document is disseminated under the sponsorship of the Department of Transportation, University Transportation Centers Program, in the interest of information exchange. The U.S. Government assumes no liability for the contents or use thereof.

1. Report No URITC FY00-08	2. Government Accession No. N/A	3. Recipient's Catalog No. N/A	
4. Title and Subtitle Effect of Microstructure on the Static and Dynamic Behavior of Recycled Asphalt Materials		5. Report Date July 2002	
		6. Performing Organization Code N/A	
7. Authors(s) Martin H. Sadd, Arun Shukla, Venkit Parameswaran and Qingli Dai		8. Performing Organization Report No.	
9. Performing Organization Name and Address  University of Rhode Island Mechanical Engineering & Applied Mechanics Department 92 Upper College Road Kingston, RI 02881		10. Work Unit No. (TRAIS) N/A	
		11. Contract or Grant No. 536138	
		13. Type of Report and Period Covered Final	
12. Sponsoring Agency Name and Address  University of Rhode Island Transportation Research Center Kingston, RI 02881		14. Sponsoring Agency Code URITC 99-38 A Study Conducted in Cooperation With the U.S. DOT	
15. Supplementary Notes N/A			
16. Abstract This report describes the research activities of a project dealing with theoretical/numerical modeling and experimental studies of the micromechanical behavior of recycled asphalt material. The theoretical work employed finite element techniques to develop a microstructural model of heterogeneous asphalt materials. The model simulates the load transfer between aggregates using a microframe network scheme whereby the binder-aggregate system is replaced by an equivalent network of finite elements. A nonlinear, softening model was developed through the use of a damage mechanics formulation. Preliminary model results compared favorably with experimental data for indirect tension tests. Experimental work included model verification studies, which investigated idealized cemented particulate systems in order to collect data on particle displacements under load. This data compared favorably with model simulation results. Indirect tension testing was also conducted for a material with a fix percentage of RAP, and preliminary visualization of IDT sample damage evolution was done. Experimental binder characterization studies were conducted on compressive and indirect tension samples.			
17. Key Words Recycled Asphalt, Finite Element Modeling, Asphalt Microstructure, Numerical Simulation		18. Distribution Statement  No restrictions. This document is available to the public through the University of Rhode Island Transportation Center, 85 Briar Lane, Kingston, RI 02881	
19. Security Classif. (of this report) Unclassified	20. Security Classif. (of this page) Unclassified	21. No. of Pages 75	22. Price N/A

Form DOT F 1700.7 (8-72) Reproduction of completed page authorized (art. 5/94)

## TABLE OF CONTENTS

	<b>Page</b>
<b>ABSTRACT</b>	<b>1</b>
<b>1. INTRODUCTION</b>	<b>2</b>
<b>2. ELASTIC ASPHALT MODEL DEVELOPMENTS</b>	<b>5</b>
<b>2.1 FEAMS Elastic Finite Element Model</b>	<b>5</b>
<b>2.2 Cementation Distribution Schemes</b>	
<b>2.2.1 Cementation Distribution - Free-Mix Conditions</b>	
<b>2.2.2 Cementation Distribution - Fully Filled Conditions</b>	
<b>2.3 Model Verification Results</b>	<b>13</b>
<b>2.3.1 ANSYS Verification</b>	
<b>2.3.2 Experimental Verification</b>	
<b>2.4 Indirect Tension Test Simulations</b>	<b>28</b>
<b>2.4.1 General Simulation Procedures</b>	
<b>2.4.2 Variable Aggregate Models</b>	
<b>3. ABAQUS ASPHALT MODEL DEVELOPMENTS</b>	<b>32</b>
<b>3.1 Elasto-Plastic Model</b>	<b>33</b>
<b>3.1.1 Basic Modeling Concept</b>	
<b>3.1.2 Elasto-Plastic Binder Properties</b>	
<b>3.2 Microframe Element Model</b>	<b>41</b>
<b>3.2.1 Elastic Analysis and Verification with FEAMS Code</b>	
<b>3.2.2 Inelastic Damage Model</b>	
<b>4. EXPERIMENTAL PROGRAM</b>	<b>56</b>
<b>4.1 Indirect Tension Testing</b>	<b>57</b>
<b>4.2 Visualization of Damage Evolution During IDT Tests</b>	<b>60</b>
<b>4.3 Characterization of Binder Strength and Stiffness</b>	<b>62</b>
<b>5. SUMMARY &amp; CONCLUSIONS</b>	<b>63</b>
<b>6. ACKNOWLEDGEMENT</b>	<b>65</b>
<b>7. REFERENCES</b>	<b>65</b>

## List of Figures

- FIGURE 1 Schematic of multi-phase asphalt materials.  
FIGURE 2 Asphalt modeling concepts.  
FIGURE 3 Idealized aggregate geometry.  
FIGURE 4 Finite element model.  
FIGURE 5 Cement layer between two particles.  
FIGURE 6 Binder distribution around minimum spacing line.  
FIGURE 7 Binder distribution for fully filled case.  
FIGURE 8 ANSYS verification model and boundary conditions for normal stiffness comparison.  
FIGURE 9 ANSYS predictions for normal stiffness verification.  
FIGURE 10 ANSYS predictions for tangential deformation.  
FIGURE 11 Compression sample configurations for two loadings  
FIGURE 12 Image analysis to extract particle displacements and rotations.  
FIGURE 13 Overall load deflection behavior of compression specimen.  
FIGURE 14 Particle displacements and rotations for 765N load increment.  
FIGURE 15 Finite element model of compression test specimen.  
FIGURE 16 Model results of particle displacements.  
FIGURE 17 Model results of particle rotations.  
FIGURE 18 Force-displacement model results of particle displacements  
FIGURE 19 Force-displacement model results of particle rotations  
FIGURE 20 Indirect tension test sample.  
FIGURE 21 Particle displacements and rotations for IDT specimen.  
FIGURE 22 Finite element model of IDT sample.  
FIGURE 23 IDT model results of particle displacements.  
FIGURE 24 IDT model results of particle rotations.  
FIGURE 25 Indirect tension test geometry.  
FIGURE 26 Typical IDT simulation behavior.  
FIGURE 27 IDT 71-particle (232 elements), variable mix model and internal force behavior.  
FIGURE 28 IDT 96-particle (286 elements), variable mix model and internal force behavior.  
FIGURE 29 Gradation comparison of IDT models with actual material.  
FIGURE 30 Comparison of IDT models for different moduli/RAP content.  
FIGURE 31 ABAQUS modeling scheme.  
FIGURE 32 Seven-particle IDT models  
FIGURE 33 FEM comparisons on the seven-particle IDT specimen.  
FIGURE 34 IDT ABAQUS computational model.  
FIGURE 35 Undeformed and deformed element meshes.  
FIGURE 36 Horizontal and vertical binder displacement contours.  
FIGURE 37 Particle displacement vector distribution.  
FIGURE 38 Particle displacement distribution showing both deformed and undeformed IDT sample.  
FIGURE 39 Particle rotation distribution.  
FIGURE 40 Von Mises stress contours.  
FIGURE 41 Horizontal normal stress contours.  
FIGURE 42 Yield stress versus equivalent plastic strain.  
FIGURE 43 Vertical force versus vertical displacement of IDT sample.  
FIGURE 44 Partial cemented verification model.  
FIGURE 45 Particle displacements (mm) – FEAMS results.

FIGURE 46 Particle displacements (mm) – ABAQUS results.  
FIGURE 47 Comparison of FEAMS and ABAQUS results.  
FIGURE 48 Full cemented verification model.  
FIGURE 49 Particle Displacements.  
FIGURE 50 Particle displacements.  
FIGURE 51 Comparison of FEAMS an ABAQUS results.  
FIGURE 52 IDT specimen showing sample failure.  
FIGURE 53 IDT load deformation data.  
FIGURE 54 Uniaxial stress-strain response for damage model.  
FIGURE 55 IDT simulation model for damage case.  
FIGURE 56 Element mesh of model shown in figure 55.  
FIGURE 57 Comparison of softening IDT models  
FIGURE 58 Comparison of damage softening IDT model with test data.  
FIGURE 59 Size gradation of virgin aggregates and sand.  
FIGURE 60 Marshall mix design for IDT test samples with 30% RAP.  
FIGURE 61 Loading fixture for indirect tensile testing.  
FIGURE 62 Load versus load-point displacement response for indirect tensile tests.  
FIGURE 63 Lateral extension versus load-point displacement for three indirect tensile tests.  
FIGURE 64 Real-time damage evolution and failure during an indirect tension test.  
FIGURE 65 Compressive stress-strain behavior for asphalt binder.  
FIGURE 66 Load versus load-point displacement response for indirect tensile test of asphalt binder elements.

## **ABSTRACT**

This report describes the second year's research activities of a project dealing with the behavior of reclaimed asphalt pavement (RAP). The project involved both theoretical/numerical modeling and experimental studies that were applied to investigate the micromechanical behavior of asphalt material.

The modeling work has employed finite element techniques to develop a microstructural model of heterogeneous asphalt materials. The model simulates the load transfer between aggregates using a microframe network scheme whereby the binder-aggregate system is replaced by an equivalent network of finite elements. Using our previously developed elastic model, the current work extended the model simulation to include nonlinear, softening behavior. This was accomplished through the use of a damage mechanics formulation which was incorporated in the microframe model and solved using the ABAQUS commercial FEA code. Preliminary model results compared favorably with experimental data for indirect tension tests.

Experimental work included model verification studies, which investigated idealized cemented particulate systems in order to collect data on particle displacements under load. This data compared well with model simulation results. Indirect tension testing was also conducted for a material with a fixed percentage of RAP, and preliminary visualization of IDT sample damage evolution was done. Experimental binder characterization studies were conducted on compressive and indirect tension samples.

## 1. INTRODUCTION

There exists considerable state, national and international interest in the use of reclaimed asphalt pavement materials (RAP). Such use of recycled materials has been occurring with varying degrees of success in the United States for the past 20 years. In 1998 the U.S. Congress established the Recycled Materials Resource Center (RMRC) at the University of New Hampshire. The purpose of the Center was to use research and outreach to reduce barriers to recycling in road construction. Recently the Federal Highway Administration completed a report by Schimmoller, et.al. (1) of a scanning tour of recycling activities in several European countries. These activities clearly indicate the strong national interest in the appropriate use of recycled products for roadways.

Both hot and cold mix recycled asphalt materials exhibit different mechanical properties when compared with new pavement product. In some cases the performance of RAP materials has not been as good, while in other cases the recycled product had better structural performance, Kandhal, et.al. (2). For Cold In-Place Recycling (CIR), recent work by Brayton, et.al. (3) has investigated performance-based mix-designs in an effort to provide information on the proper use of such materials. However, there still exists uncertainty on proper recycling processes and on the subsequent performance of the recycled product. Asphalt is a complex heterogeneous material composed of aggregate, binder/cement, additives and void space. Recycling processes further complicate the mechanical behavior by introducing additional variation of these constituents, and by adding several ageing/time-dependent effects such as hardening, chemical oxidation and binder microcracking. A fundamental understanding of the material behavior is needed to help understand and explain recycling issues, and a micromechanical model would be best to establish such basic mechanisms.

Asphalt pavements must withstand a wide variety of loading and temperature conditions. For example, traffic loadings can vary from quasi-static to dynamic impact, and pavement breakdown commonly occurs as a result of strength (stress), fracture and/or fatigue failure, and time dependent deformation (creep-rutting). Previous studies on the failure and fracture behaviors of asphalt and bituminous cements include the work of Salam and Monismith (4), Majidzaheh and Kauffmann (5), Majidzadeh et.al. (6), Karakouzian and Majidzadeh (7), Sousa and Monismith (8), Tschegg, et.al.(9), and Mobasher, et.al.(10). With regard to recycled materials, Sulaiman and Stock (11) have conducted fracture experiments on RAP materials with varying amounts of recycled constituent. Recently Venkatram (12) conducted a series of fracture and dynamic impact experiments on RAP materials.

Because asphalt is a multiphase-heterogeneous material, previous studies focusing on the continuum response cannot be used to describe the micromechanical behavior between aggregate and binder. Recently some studies have been investigating the micromechanical behaviors of particulate, porous and heterogeneous materials. For example, studies on cemented particulate materials by Dvorkin et.al. (13) and Zhu et.al. (14,15) provide information on the load transfer between particles which are cemented together. Such mechanics provide details on the normal and tangential interparticle load transfer, and would be fundamental in developing a micromechanical theory for load distribution and failure of such materials. Some contact-based analysis of asphalt performance has recently been reported by Chang and Gao (16), Cheung, et.al. (17), and Zhu et.al. (18,19). Using mixture theory, Krishnan and Rao (20) presented a multi-phase approach to explain air void reduction in asphalt materials under load.

Recent numerical modeling of cemented particulate materials has generally used two particular simulation schemes. The first method uses *finite element* procedures to establish the load carrying behavior between the particles. A second general approach incorporates the

*discrete element method*, which models the individual motion of each particle in model granular systems.

Discrete element modeling studies on cemented particulate materials include the work by Rothenburg, et.al. (21), Chang and Meegoda (22), Trent and Margolin (23), Buttlar and You (24) and Ullidtz (25). Sadd et.al. (26,27) have also used this scheme to numerically investigate the dynamic response of cemented and damaged granular materials.

In regard to finite element modeling (FEM), Stankowski (28) applied standard FEM techniques to cemented particulate composites. Sepehr et.al. (29) used an idealized finite element microstructural model to analyze the behavior of an asphalt pavement layer. A common finite element approach to simulate particulate and heterogeneous materials has used the idea of representing the interparticle behavior using an *equivalent lattice network system*. This type of microstructural modeling has been used previously; Bazant, et al. (30), Mora (31), Sadd et al. (32) and Budhu, et al. (33). Along similar lines, Guddati, et al. (34) recently presented a random truss lattice model to simulate microdamage in asphalt concrete and demonstrated some interesting failure patterns in an indirect tension test geometry. Bahia et al. (35) have also used finite elements to model the aggregate-binder response of asphalt materials, and Papagiannakis, et al. (36) have conducted similar studies for the viscoelastic response. Mustoe and Griffiths (37) developed a finite element model, which was equivalent to a particular discrete element approach. They pointed out that the FEM model has an advantage over the discrete element scheme for static problems.

As a result of the past modeling work, the finite element scheme appeared to be most suited for asphalt simulation, and a two-dimensional, elastic FEM model was developed in the first year of this research program. Sadd and Dai (38), Sadd, et.al.(39, 40) have reported on this model development and have given some preliminary simulation results.

Based on this approach, additional model construction has been accomplished during the second year of the research program. This new work has extended the original elastic model and enhanced the material generating scheme. Based on a damage mechanics approach, a new non-linear finite element procedure has been developed and incorporated within the ABAQUS FEA code. The new model gives nonlinear, softening behaviors commonly observed in asphalt samples. Also during the second year of the research program, experimental studies have been conducted on model verification, indirect tension testing, damage evolution monitoring and binder stiffness and strength characterization. Results of each of these tasks will be presented in the following sections.

## **2. ELASTIC ASPHALT MODEL DEVELOPMENTS**

### **2.1 FEAMS Elastic Finite Element Model**

Shown in Figure 1, bituminous asphalt is commonly described as a multi-phase material containing aggregate, binder cement (including mastic and fine particles) and air voids. The load transfer between the aggregates plays a primary role in determining the load carrying capacity and failure of such complex materials. A micromechanical model of such materials must properly account for the load transfer between all aggregates in the cemented particulate system. The aggregate material is normally much stiffer than the binder, and thus aggregates are to be modeled as rigid particles. In order to properly account for the load transfer between aggregates in an idealized system, we assume that there is an effective binder zone between neighboring particles. It is through this zone that the micro-mechanical load transfer occurs between each aggregate pair. This loading can be reduced to a resultant force and moment system as shown in Figure 1. The resultant force loading on a given aggregate can be decomposed into normal and tangential components with respect to a coordinate system parallel and perpendicular to a line connecting the aggregate mass centers.

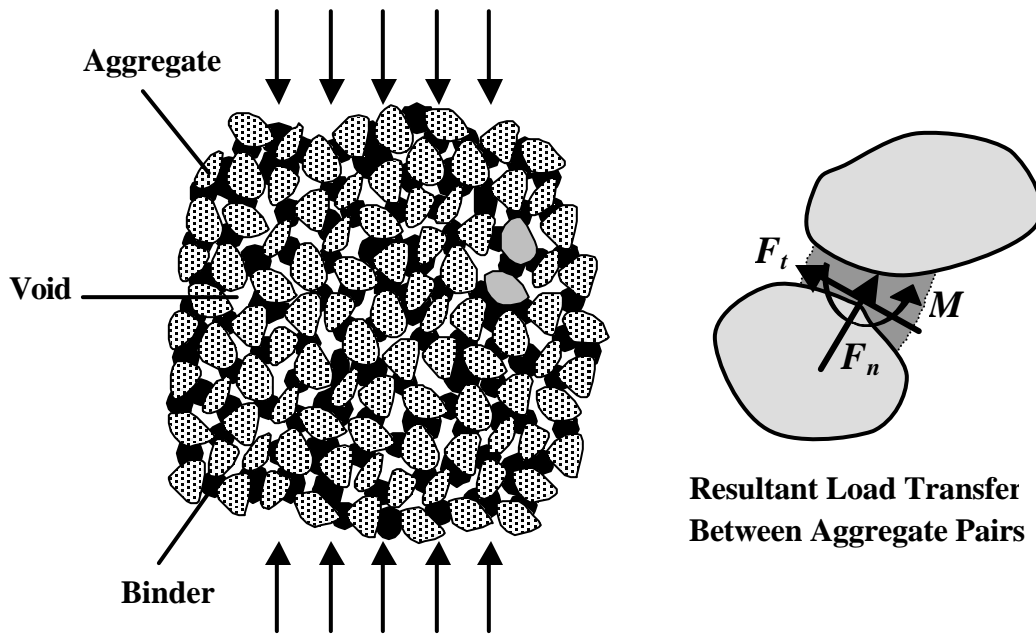


**FIGURE 1 Schematic of multi-phase asphalt materials.**

In order to develop such a micromechanical model, some simplifying assumptions must be made about allowable aggregate shape and the binder geometry. Aggregate geometry has been studied for many years, and recently some work has been conducted on quantifying particle size, shape, angularity and texture. However, for the present modeling only size and shape will be considered. In general, asphalt concrete contains aggregate of very irregular geometry as shown in Figure 2(a). Our approach is to allow variable size and shape using a simple elliptical aggregate model as represented in Figure 2(b). Using the equivalent lattice network approach, a finite element scheme is developed to simulate this interparticle load transfer using a frame-type of element. Such a modeling scheme would then replace the cemented aggregate system with a network of specially created finite elements connected at the aggregate mass centers, as shown in Figure 2(c). Our first year report, Sadd and Dai (38), provides details on this modeling scheme.

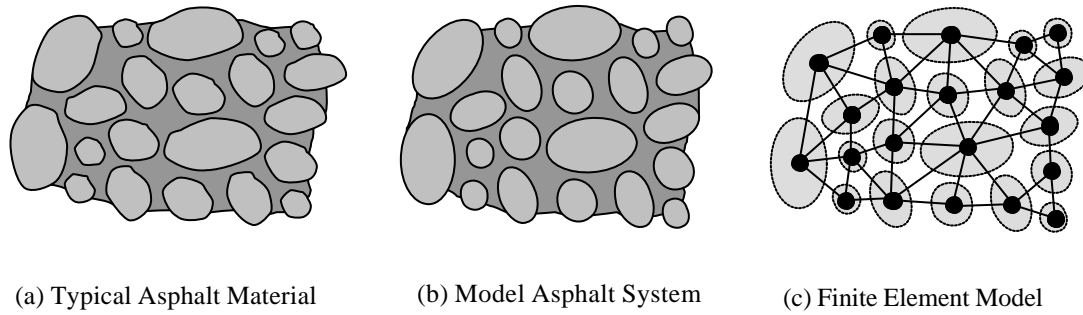


**FIGURE 2 Asphalt modeling concepts.**

In order to generate model materials, several geometric aggregate and binder properties are needed. Figure 3 illustrates a typical particle pair, and each idealized elliptical aggregate is characterized by shape measures  $a_i$  and  $b_i$ , and location and orientation with respect to a global coordinate system. The finite element lies along the *branch vector* defined as the line connecting particle mass centers. The effective binder area is defined as a strip of cementation material parallel to the branch vector as shown. By varying the cementation widths  $w_1$  and  $w_2$ , different amounts and distributions of binder can be created within the numerical model.

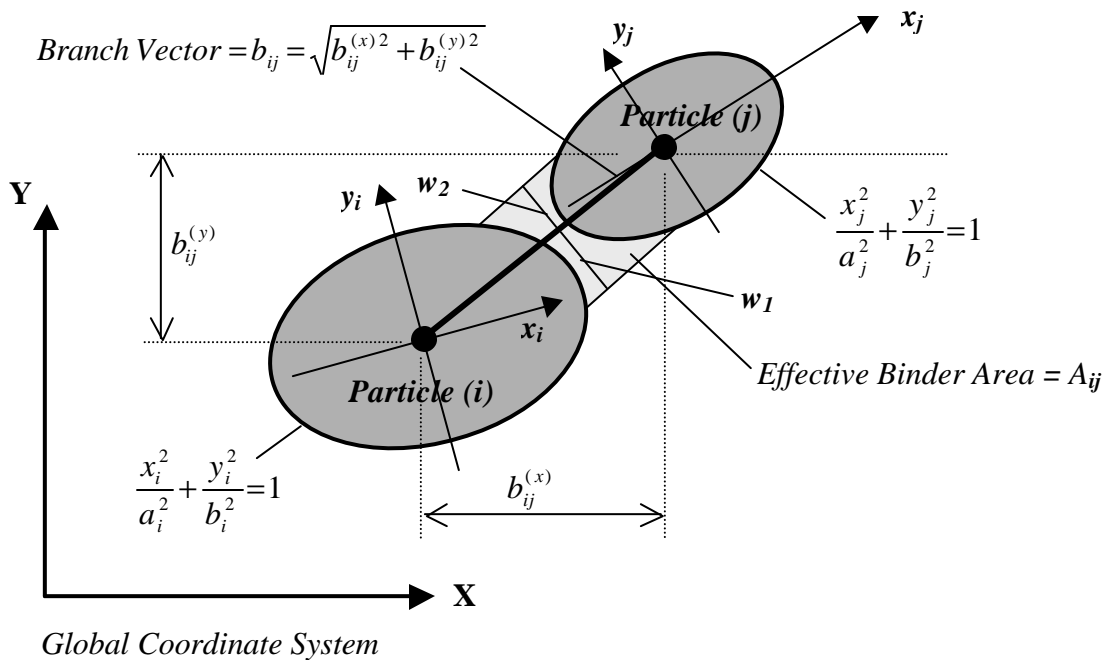


**FIGURE 3 Idealized aggregate geometry.**

The interparticle load transfer is modeled by using a specially developed, six degree-of-freedom frame-type finite element as shown in Figure 4. Nodal displacements and rotations correspond to the aggregate mass center motions.

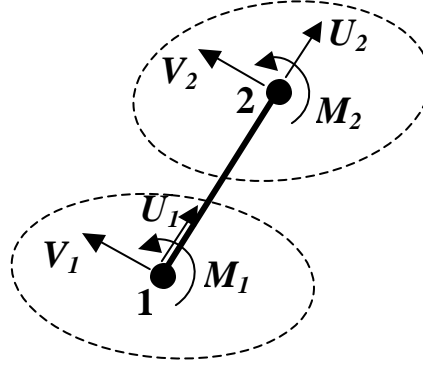


**FIGURE 4 Finite element model.**

The general element equation for this case may be expressed as

$$\begin{bmatrix} K_{11} & K_{12} & K_{13} & K_{14} & K_{15} & K_{16} \\ \cdot & K_{22} & K_{23} & K_{24} & K_{25} & K_{26} \\ \cdot & \cdot & K_{33} & K_{34} & K_{35} & K_{36} \\ \cdot & \cdot & \cdot & K_{44} & K_{45} & K_{46} \\ \cdot & \cdot & \cdot & \cdot & K_{55} & K_{56} \\ \cdot & \cdot & \cdot & \cdot & \cdot & K_{66} \end{bmatrix} \begin{Bmatrix} U_1 \\ V_1 \\ \theta_1 \\ U_2 \\ V_2 \\ \theta_2 \end{Bmatrix} = \begin{Bmatrix} F_{n1} \\ F_{t1} \\ M_1 \\ F_{n2} \\ F_{t2} \\ M_2 \end{Bmatrix} \quad (1)$$

For a usual frame element, the various stiffness terms  $K_{ij}$  are determined using standard uniaxial bar and Euler-Bernouli or Timoshenko beam theory. However, for our particular application, the asphalt cement cannot be modeled by simple bar or beam action. A more complete stress analysis within the binder material is need, and this has been determined from an approximate elasticity solution originally developed by Dvorkin et.al.(13). This work provides a simple analytical solution for the stress distribution in a cement layer between two particles. We use the special case where the particle material stiffness is much greater than that of the cement layer,

and thus the particles are assumed to be rigid. For the uniform cement thickness case Dvorkin's two-dimensional model is based on the geometry shown in Figure 5.

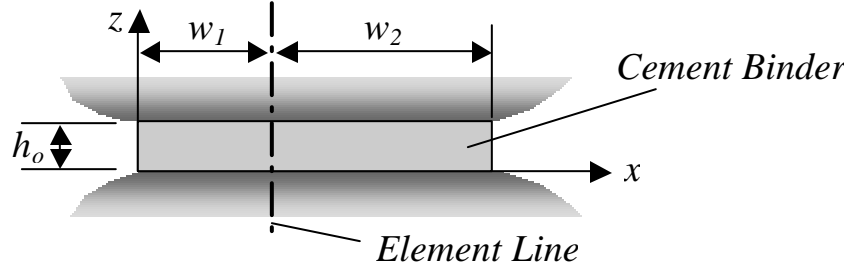


**FIGURE 5 Cement layer between two particles.**

The stresses  $\sigma_x$ ,  $\sigma_z$  and  $\tau_{xz}$  within the cementation layer can be calculated for particular relative particle motion cases involving normal, tangential and rotational cases. These stresses can then be integrated to determine the total load transfer within the cement binder, thus leading to the calculation of the various stiffness terms in relation (1). The details of this process have been previously reported by Sadd and Dai (38), and the final result is given by

$$[K] = \begin{bmatrix} K_{nn} & 0 & K_{nn}e & -K_{nn} & 0 & -K_{nn}e \\ 0 & K_{tt} & K_{tt}r_1 & 0 & -K_{tt} & K_{tt}r_2 \\ K_{nn}e & K_{tt}r_1 & K_{tt}r_1^2 + \frac{K_{nn}}{3}(w_2^2 - w_1w_2 + w_1^2) & -K_{nn}e & -K_{tt}r_1 & K_{tt}r_1r_2 - \frac{K_{nn}}{3}(w_2^2 - w_1w_2 + w_1^2) \\ -K_{nn} & 0 & -K_{nn}e & K_{nn} & 0 & K_{nn}e \\ 0 & -K_{tt} & -K_{tt}r_1 & 0 & K_{tt} & -K_{tt}r_2 \\ -K_{nn}e & K_{tt}r_2 & K_{tt}r_1r_2 - \frac{K_{nn}}{3}(w_2^2 - w_1w_2 + w_1^2) & K_{nn}e & -K_{tt}r_2 & K_{tt}r_2^2 + \frac{K_{nn}}{3}(w_2^2 - w_1w_2 + w_1^2) \end{bmatrix} \quad (2)$$

where  $K_{nn} = (\lambda + 2\mu)w/h_o$ ,  $K_{tt} = \mu w/h_o$ ,  $\lambda$  and  $\mu$  are the usual elastic moduli,  $e = (w_2 - w_1)/2$ , and  $r_1$  and  $r_2$  are the radial dimensions from each aggregate center to the cementation boundary.

In order to simulate the micromechanical behavior of asphalt materials, it is necessary to create particular idealized asphalt materials with appropriate microstructural geometry such as the size, shape and distribution of the aggregates, binder and voids. The *Asphalt Material Generator* (AMGEN) code (38) developed during first year of the project, provides a

controllable numerical scheme to create a variety of model asphalt materials. The code creates and spatially distributes aggregate particles of circular or elliptical shape in regular or random distributions. Rectangular areas of binder material of particular geometry and mechanical moduli are then created between appropriate neighboring particles. The generating code also develops model geometric and material property files needed as input to the simulation code.

The previous theoretical developments have been incorporated into a special purpose finite element simulation code, **Finite Element Asphalt Material Simulation (FEAMS)**. The code uses the two-dimensional micro-frame concept as shown in Figure 2(c) with the stiffness matrix given by equation (2). The generating and simulation codes then allow numerical simulation experiments to be conducted on a variety of model materials.

## **2.2 Cementation Distribution Schemes**

In order to apply the modeling to particular asphalt materials, the material generating code must create binder distributions between appropriate particles in the idealized model system as shown in Figure 3. During hot mixing conditions, the deformation and flow of molten asphalt (mastic) plus the associated fine materials is governed by some rather complex physics. Issues of surface adhesion, capillary action, mixing and consolidation conditions along with other effects make the determination of binder deposition difficult to predict with precision. We have therefore made some assumptions for particular cases and have developed two distribution schemes as described below.

### **2.2.1 Cementation Distribution - Free-Mix Conditions**

The physics of free capillary and surface adhesion would tend to suggest that the binder cement between aggregates would be approximately centered around a line through the minimum spacing distance as shown below. This would produce a nonuniform cement distribution with respect to the branch vector as indicated. In order to calculate the binder widths

$w_1$  and  $w_2$ , it is necessary to determine the location of this minimum spacing line. This location is a function of the locations, orientations and sizes of particular particle pairs.

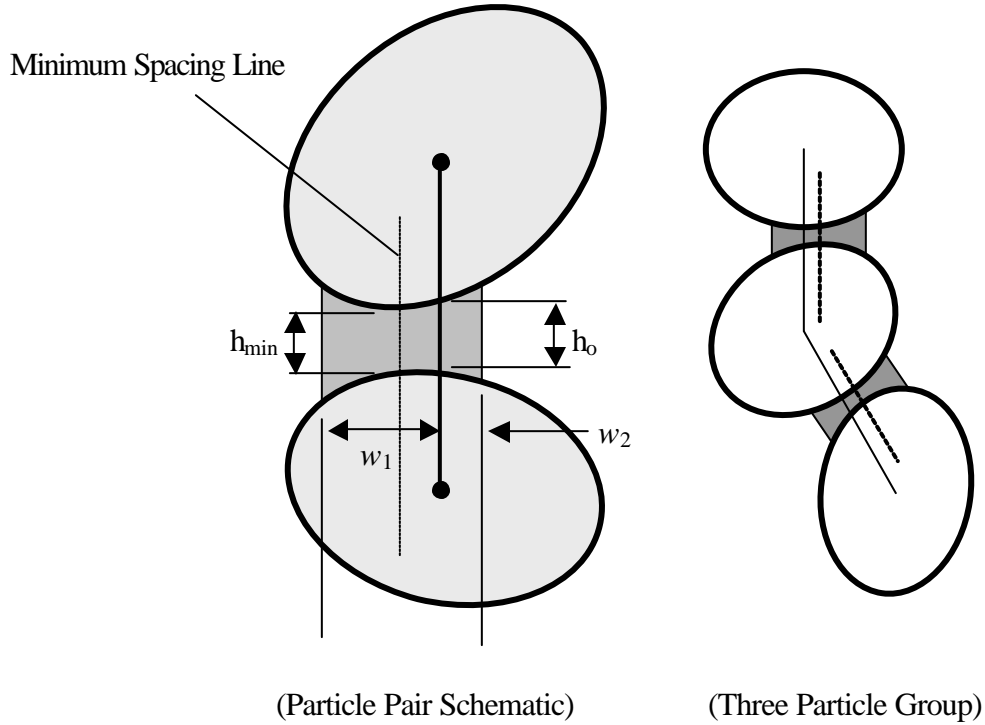


**FIGURE 6 Binder distribution around minimum spacing line.**

### 2.2.2 Cementation Distribution - Fully Filled Conditions

For the case of a fully filled matrix cement distribution, there exists a total cement bridge between particle pairs (i,j) as shown in Figure 7. In order to develop a relatively simple means to determine the binder widths, a perpendicular to the associated branch vector is drawn at each particle center. This line establishes widths  $w_i$  and  $w_j$  as shown. The binder widths are then taken as the average value of these dimensions, i.e.

$$w_1 = w_2 = \frac{1}{2}(w_i + w_j) \quad (3)$$

Due to the geometry variation for this case, we have also modified the binder thickness parameter  $h_0$ , as originally defined in Figure 5. The binder thickness is modeled approximately by assuming different (but constant) binder thickness on each side to the branch vector as shown in Figure 7. The values of  $h_1$  and  $h_2$  are determined by the average thickness values on each side of the branch vector. This modification requires new calculation of particular element stiffness values in the matrix given in equation (2). In particular,

$$\begin{aligned}
 K_{nn} &= (\lambda + 2\mu)w \left( \frac{1}{h_1} + \frac{1}{h_2} \right) \\
 K_{tt} &= \mu w \left( \frac{1}{h_1} + \frac{1}{h_2} \right) \\
 K_{nr} &= \frac{(\lambda + 2\mu)}{2} w^2 \left( \frac{1}{h_2} - \frac{1}{h_1} \right) \\
 K_{rr} &= M_{rn} \pm M_{rt} \\
 M_{rn} &= \frac{(\lambda + 2\mu)}{3} w^3 \left( \frac{1}{h_1} + \frac{1}{h_2} \right) \\
 M_{rt} &= K_{tt} r_i r_j
 \end{aligned} \tag{4}$$

where  $r_i$  and  $r_j$  are defined similarly as in equation (2).

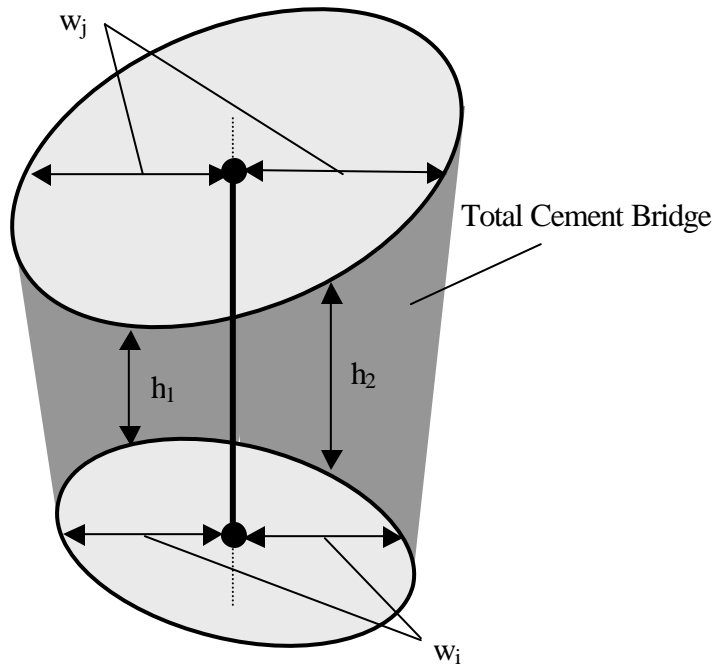


**FIGURE 7 Binder distribution for fully filled case.**

## 2.3 Model Verification Results

Verification of the developed model has been made through simulation comparisons with both an independent finite element code (ANSYS) for a simple loading condition and with experimental data on an idealized material system.

### 2.3.1 ANSYS Verification

#### *Normal Stiffness Verification*

Normal stiffness predictions from our micromechanical model were compared with those determined from the commercial ANSYS finite element code. The ANSYS model for this case is shown in Figure 8, and was composed of two circular particles ( $r_1 = r_2 = 5.5mm$ ) connected by a symmetric cement binder with geometry  $w_1 = w_2 = 3.0mm$  and average thickness  $h_0 = 3.89mm$ . The binder elastic constants were chosen as  $E = 1.0MPa$ ,  $\nu = 0.3$  and the particle constants were  $E = 1.0GPa$ ,  $\nu = 0.3$ . Note the particle stiffness is three orders of magnitude higher than that of the binder, thus being consistent with the assumption of rigid aggregates.

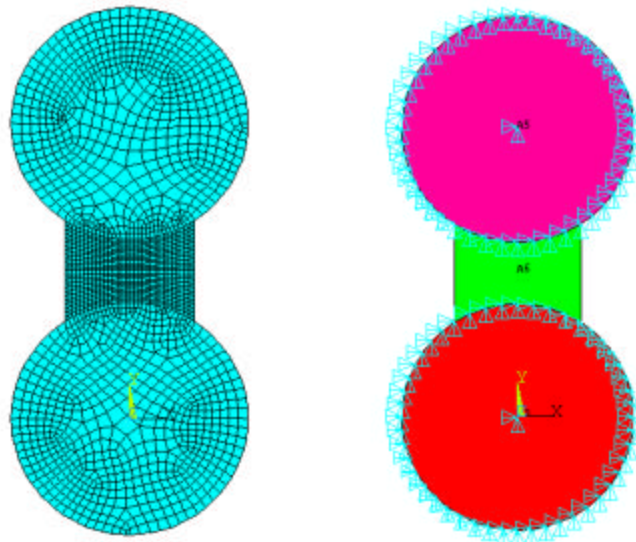


**FIGURE 8 ANSYS verification model and boundary conditions for normal stiffness comparison.**

This ANSYS model used displacement boundary conditions where all nodes were fixed on the bottom particle, while the top particle had all nodes displaced vertically at amount  $\Delta y$ . Plane strain, 8-noded quadratic elements were used to mesh and analyze the problem.

The ANSYS finite element predictions for this elastic normal stiffness verification case are shown in Figure 9. The left figure illustrates the deformed configuration, while the right figure shows the vertical displacement contours within the binder cement.

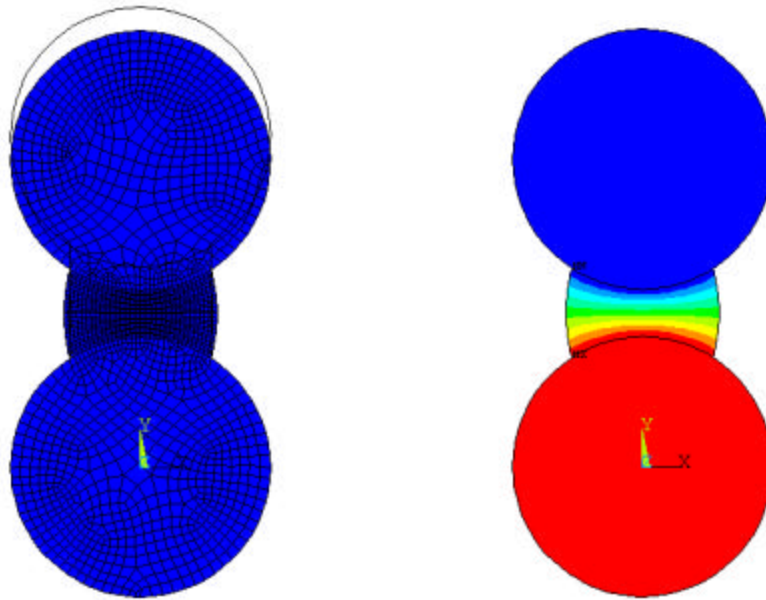


**FIGURE 9 ANSYS predictions for normal stiffness verification.**

In order to calculate the vertical load transfer through the binder, the vertical nodal forces were summed for nodes along the boundary between the top particle and the binder mass. This force was then divided by the top particle vertical displacement to determine the normal stiffness giving the result  $(K_{nn})_{FEM} = F_y / \Delta y = 997 / 0.5E - 3 = 1.994 MPa$ . Using the micro-frame element model, the normal stiffness was calculated as  $(K_{nn})_{Micro} = (\lambda + 2\mu)w / \bar{h} = 2.076 MPa$ . Thus the absolute error in normal stiffness is  $\Delta K_{nn} = |(K_{nn})_{FEM} - (K_{nn})_{Micro}| = 0.082 MPa$ , and the relative error is given by

$$\frac{\Delta K_{nn}}{(K_{nn})_{Micro}} = \left| \frac{(K_{nn})_{FEM} - (K_{nn})_{Micro}}{(K_{nn})_{Micro}} \right| = 3.95\%.$$

These results indicate very good comparisons between the two models.

### *Tangential Stiffness Verification*

For the tangential case the ANSYS model had the same geometry and mesh as before (see Figure 8). The boundary conditions for this case had the bottom particle fixed as before, while the nodes of the top particle had zero vertical displacement and a prescribed uniform horizontal displacement  $\Delta x$ . The ANSYS predictions for the tangential deformation are shown in Figure 10. The left figure illustrates the deformed configuration, while the right figure shows the tangential displacement contours in the binder material.

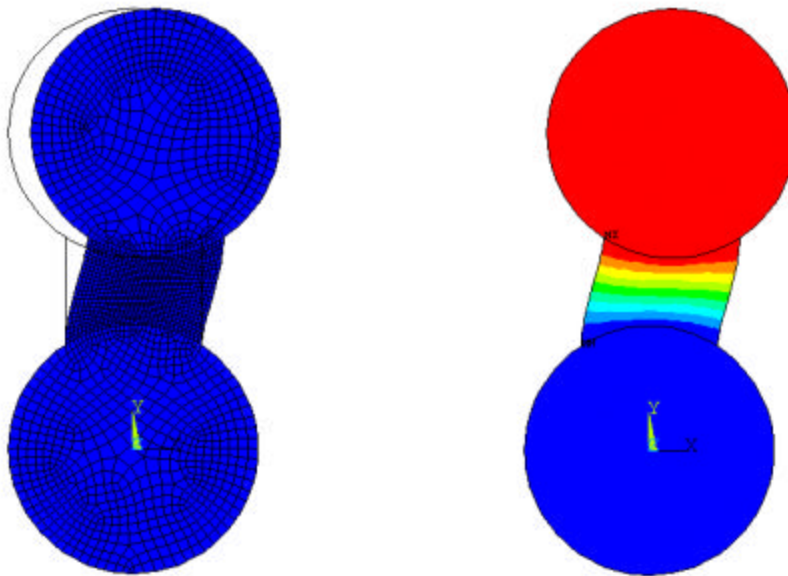


**FIGURE 10 ANSYS predictions for tangential deformation.**

As in the previous normal stiffness calculation, the horizontal (tangential) nodal forces along the boundary between the top particle and the binder were summed to get the total

tangential transferred force. Dividing this force by the horizontal displacement gives the tangential stiffness as  $(K_{tt})_{FEM} = F_x / \Delta x = 276 / 0.5E - 3 = 0.552MPa$  . Using the micro-frame model, the tangential stiffness was calculated as  $(K_{tt})_{Micro} = \mathbf{m}w / \bar{h} = 0.592MPa$  . Thus the absolute error for tangential stiffness is  $\Delta K_{tt} = |(K_{tt})_{FEM} - (K_{tt})_{Micro}| = 0.04$  Mpa, and the relative error becomes

$$\frac{\Delta K_{tt}}{(K_{tt})_{Micro}} = \left| \frac{(K_{tt})_{FEM} - (K_{tt})_{Micro}}{(K_{tt})_{Micro}} \right| = 6.7 \%$$

These results again show good comparison thus indicating that the micromechanical model predictions appear to match well with ANSYS results for the elastic case.

### **2.3.2 Experimental Verification**

In order to further verify the finite element simulation code, experiments were conducted on two types of idealized asphalt models. The idealized specimens were cast plates of soft polyurethane matrix with embedded aluminum particles fabricated in geometries to simulate standard compression and indirect tension tests.

#### ***Compression Sample***

The first verification sample was fabricated in a rectangular shape to be used as a compression test. The sample consisted of 25 elliptical particles arranged in random locations in a polyurethane matrix as shown in Figure 11. Consistent with the modeling assumptions, the stiffness of the aluminum particles (aggregate) was several orders of magnitude higher than that of the matrix (binder cement). The particles were fabricated to an elliptical shape (19 x 12.2mm) on a CNC milling machine. An acrylic mold (150 x 150 x 12mm) was prepared with inner surfaces lined with 0.18 mm thick Mylar sheets and sprayed with mold release to facilitate separation of the cast specimens. The particles were arranged in a random pattern in the mold,

and a two-part Hapflex 500 series polyurethane was used as the matrix cement. The matrix mix was degassed in a vacuum chamber to remove entrapped air. The mixture was preheated in a microwave oven to reduce its viscosity and then poured into the mold around the aluminum particles. The system was then allowed to cure for 24 hours. A sample of the matrix material was tested independently to determine the elastic compressive modulus of  $E = 4.5\text{-}5.0\text{MPa}$ , while the value of Poisson's ratio was estimated from previously published data as  $\nu = 0.48$ . The aggregate volume fraction for this sample was 28%.

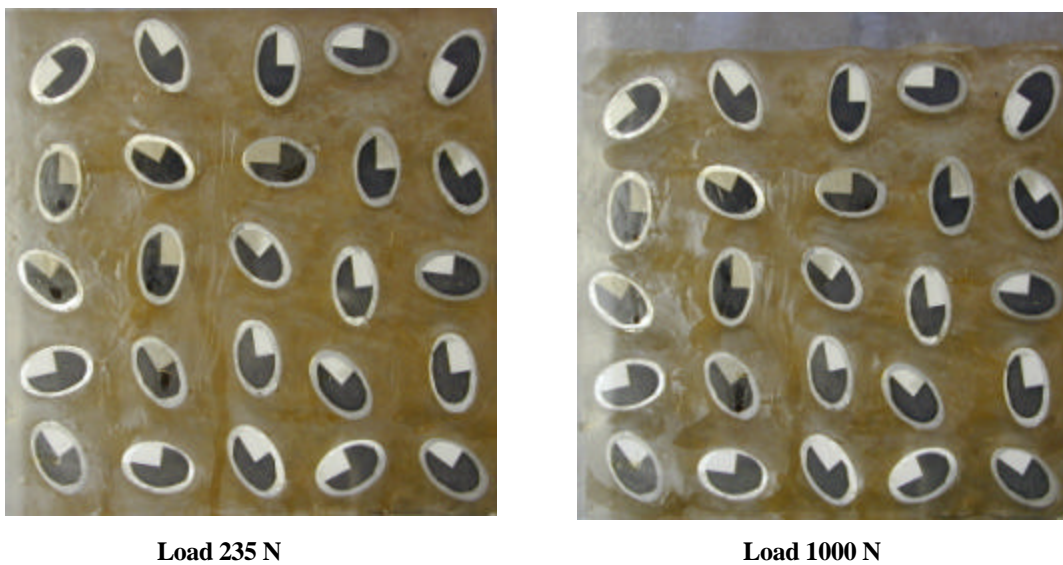


**FIGURE 11 Compression sample configurations for two loadings.**

In order to track their displacement and rotation during loading, all particles were tagged with two perpendicular high contrast markers. The specimen was placed between two Plexiglas sheets in order to prevent out-of-plane motion. The surfaces of the specimen were lubricated with a thin film of oil to reduce frictional constraints and allow free deformation. The specimen was loaded in compression on the top edge using an Instron testing machine and specimen photographs for two particular loadings are shown in Figure 11.

In order to determine the particle movements, the photographs were analyzed using an image analysis software code written in MATLAB. The image analysis code was used to detect the edges of the

particle markers and clean any stray pixels. The code locates about 20 to 30 points on the two perpendicular edges of the particle marker and fits a line through these points using a least squares method. This helps to reduce digitizing errors by averaging the data. The intersection point of the two lines then determines the particle center, and the angular orientation of the lines provides information on the particle rotation. Some of the image processing steps are shown in Figure 12.

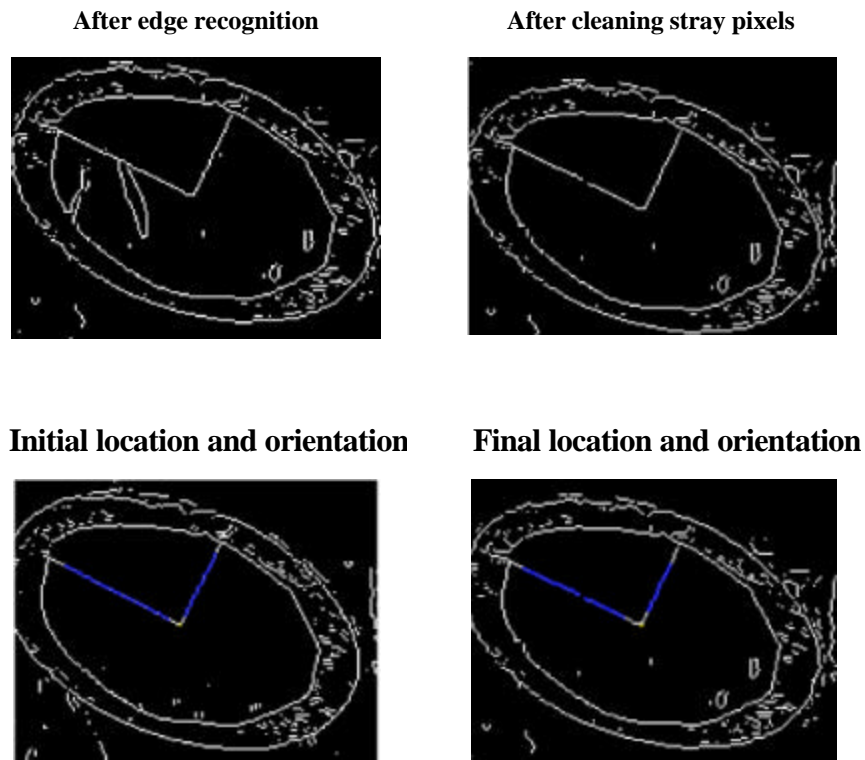


**FIGURE 12 Image analysis to extract particle displacements and rotations.**

The overall load-deflection response of the tested polyurethane sample is shown in Figure 13. The data shows slight initial nonlinearity up to about 235N, followed by approximately linear behavior up to 1000N. The particle displacements and rotations between the 235N and 1000N loadings are shown in Figure 14. It can be observed that the vertical displacements increase from bottom to the top since the sample is fixed at the bottom. Horizontal displacements are not symmetric, and this is due to the nonsymmetry in the particle arrangements. Particles whose

major axes were aligned with the loading direction had the least amount of rotation. In general, disk rotations occurred in such a way as to bring the major axis normal to the loading direction.

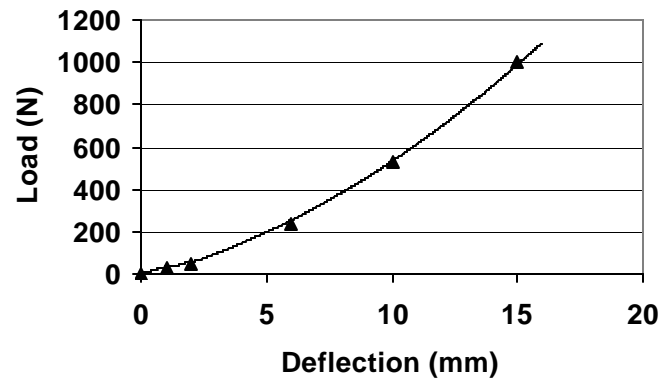


**FIGURE 13 Overall load deflection behavior of compression specimen.**

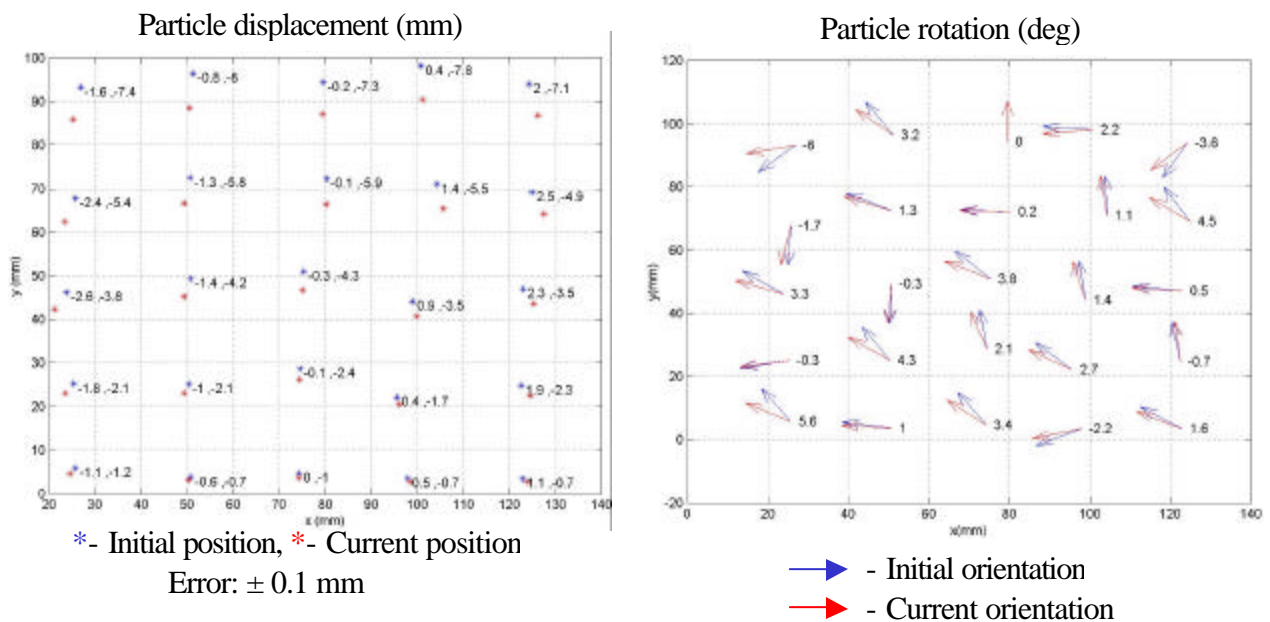


**FIGURE 14 Particle displacements and rotations for 765N load increment.**

Using our finite element modeling code FEAMS, a numerical simulation of this experiment was conducted. The 765N load increment (from 235-1000N) shown in Figure 11, was modeled using identical particles in the measured positions. The AMGEN code generated

the appropriate simulation model with 25 particles and 72 binder elements as shown in Figure 15. The cement-binder widths were made equal to 60% of the minimum projected particle axis perpendicular to each of the respective branch vectors, and the eccentricity was taken as  $e = (w_2 - w_1)/2 = 0.2$ . The model thickness was 12.5mm to match the experimental specimen dimension. Mechanical moduli of the binder cementation were chosen to match values of the polyurethane, i.e.  $E = 5\text{MPa}$  and  $\nu = 0.48$ .

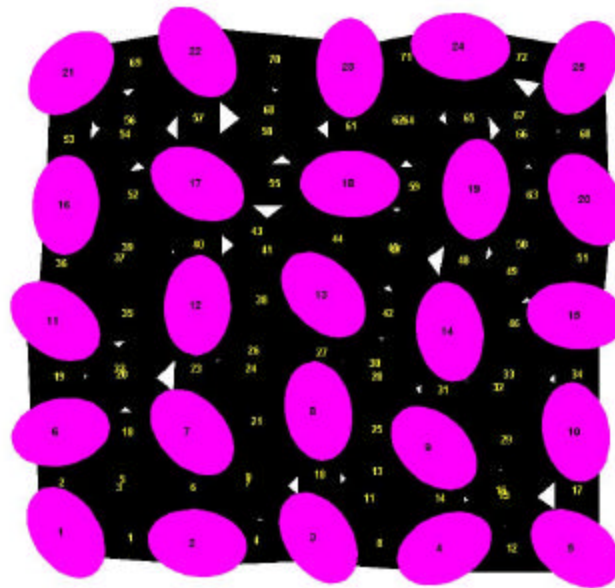


**FIGURE 15 Finite element model of compression test specimen.**

The actual experiment involved specimen loading through the boundary matrix material (see Figure 11), whereas the simulation code handles boundary loading only through nodal forces or displacements applied at particular particle centers. Because of this, two different modeling approaches were used to approximately simulate the experiment.

#### *Displacement Model*

For this model, boundary particle displacements from the experiment were specified, and interior particle motions and the total compressive force were predicted. Thus, experimental values of the particle displacements and rotations were specified on the top and bottom rows of

the model in Figure 15. Horizontal particle displacements along the right and left edges were also specified. The model results of the particle displacements and rotations are given in Figures 16 and 17.

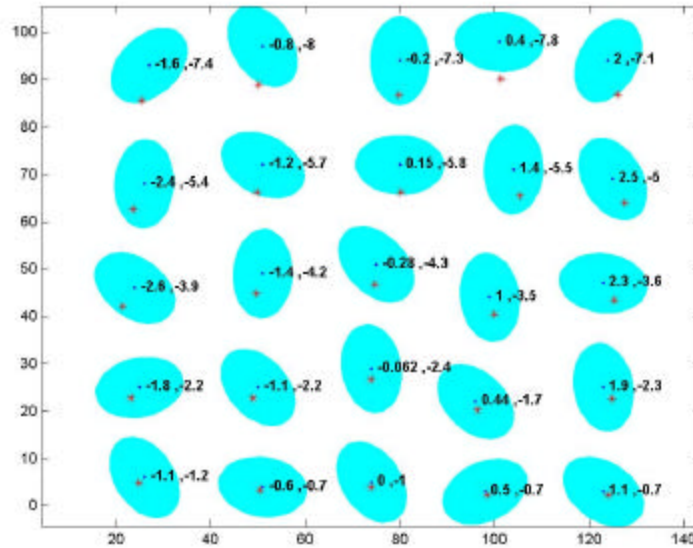


**FIGURE 16** Model results of particle displacements (mm)  
(C initial position, \* final position).

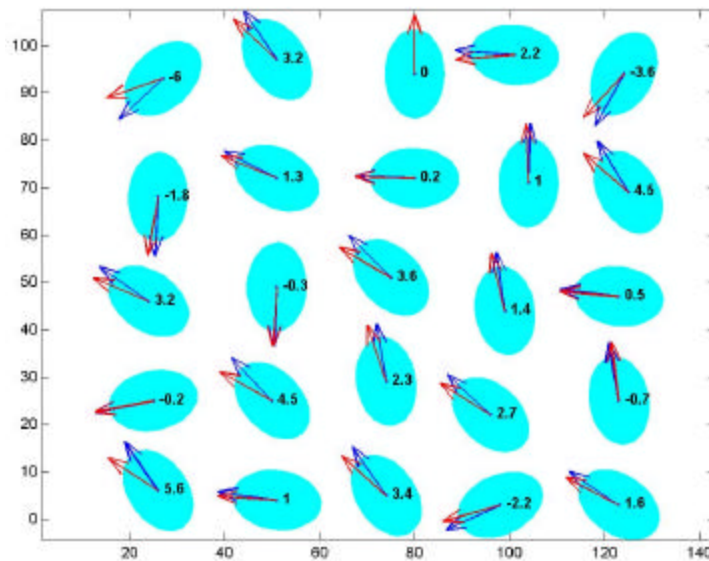


**FIGURE 17** Model results of particle rotations (deg, +ccw).

The average error between the experimental data and model predictions are specified by the relations

$$\begin{aligned}
 X_{error} &= \frac{\sum_{i=1}^9 |X_i^{FEM} - X_i^{EXP}|}{\sum_{i=1}^9 |X_i^{EXP}|} \times 100 = 6.5\% \\
 Y_{error} &= \frac{\sum_{i=1}^{15} |Y_i^{FEM} - Y_i^{EXP}|}{\sum_{i=1}^{15} |Y_i^{EXP}|} \times 100 = 1.6\% \\
 \theta_{error} &= \frac{\sum_{i=1}^{15} |\theta_i^{FEM} - \theta_i^{EXP}|}{\sum_{i=1}^{15} |\theta_i^{EXP}|} \times 100 = 3.9\%
 \end{aligned} \tag{5}$$

Summing the vertical nodal forces along the top edge of the model resulted in a total force of 723N. It was expected that this model result for the total load would be less than the experimental value of 765N because some of the actual load is transferred directly through the matrix material (e.g. along the right and left edges of the specimen). This matrix load transfer is not accounted for in the current finite element model.

#### *Force-Displacement Model*

A second modeling approach used a combination of particular boundary displacements and forces. For this case, the particular nodal forces from the previous model were used as boundary conditions along the top edge of the specimen. As in the previous case, experimental nodal (particle) displacements and rotations were used as boundary conditions along the bottom and vertical sides. The model results of the particle displacements and rotations are given in Figures 18 and 19.

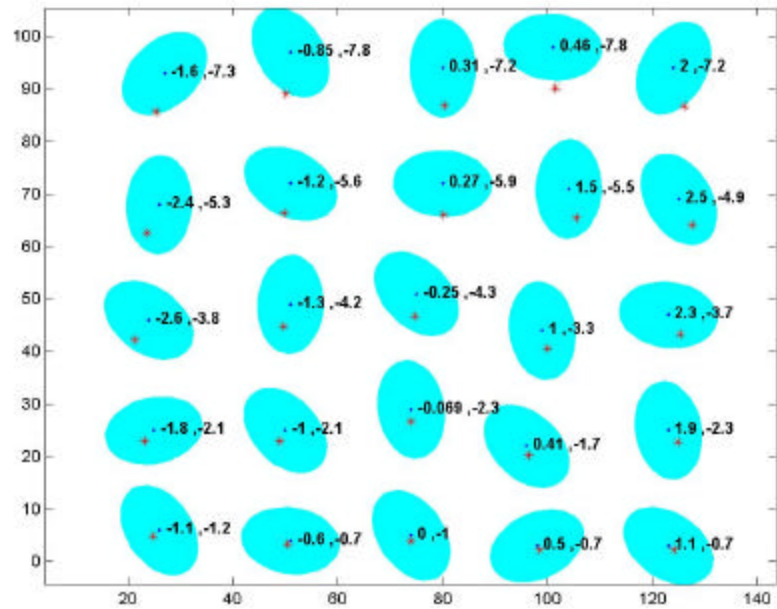


**FIGURE 18** Force-displacement model results of particle displacements (mm)  
(C initial postion, \* final position).

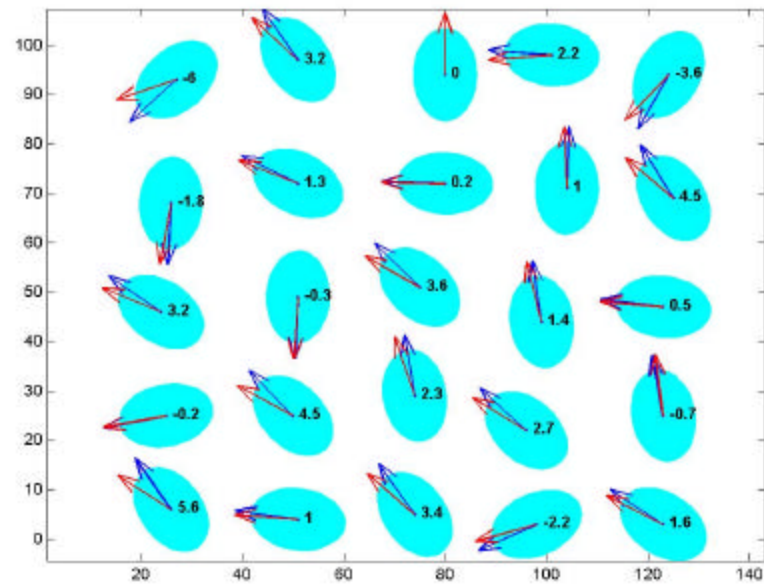


**FIGURE 19** Force-displacement model results of particle rotations (deg, +ccw).

For this model, the average error between experimental data and model predictions are given by

$$\begin{aligned}
 X_{error} &= \frac{\sum_{i=1}^{12} |X_i^{FEM} - X_i^{EXP}|}{\sum_{i=1}^{12} |X_i^{EXP}|} \times 100 = 7.2\% \\
 Y_{error} &= \frac{\sum_{i=1}^{20} |Y_i^{FEM} - Y_i^{EXP}|}{\sum_{i=1}^{20} |Y_i^{EXP}|} \times 100 = 1.4\% \\
 \theta_{error} &= \frac{\sum_{i=1}^{20} |\theta_i^{FEM} - \theta_i^{EXP}|}{\sum_{i=1}^{20} |\theta_i^{EXP}|} \times 100 = 3.1\%
 \end{aligned} \tag{6}$$

For both comparison cases, the finite element simulations compared favorably with the experimental data. However, due to the unknown nature of the applied external loading, the boundary conditions used in the modeling were not those experienced in the experiments. Therefore to provide a more definitive comparison, another type of verification model sample was created.

### ***Indirect Tension Sample***

The second experimental verification test was conducted on an indirect tension geometry as shown in Figure 20. We will use the terminology IDT for this test. The circular sample had a diameter of 125mm and was prepared such that a compressive load could be applied on two diametrically opposite particles. This type of loading produces a tensile splitting stress field at interior points along the loaded diameter. The sample consisted of 37 particles of circular and elliptical shape randomly arranged as shown. The elliptical particles had the same dimensions as used in the previous compression sample, while the circular particles had a diameter of 15mm. The aggregate volume fraction of this sample was 47.5 %. Sample materials, fabrication, loading preparation and particle measuring systems were all identical to the previous case.

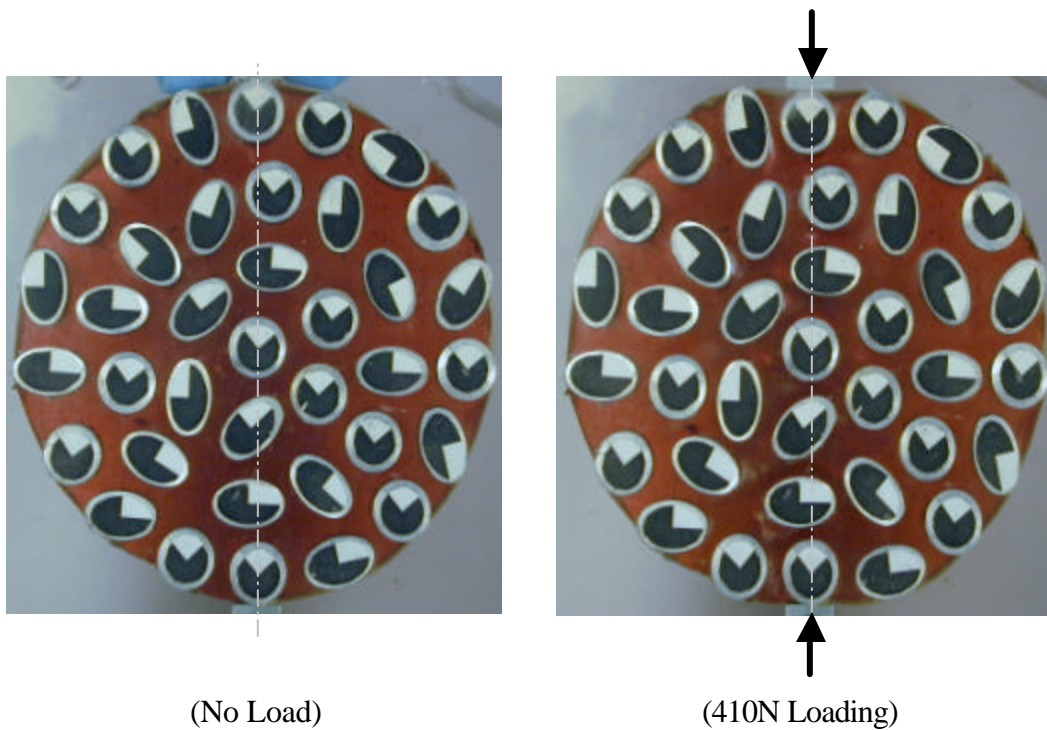


**FIGURE 20 Indirect tension test sample.**

The sample was loaded through bearing blocks with a 410N compressive force as shown in Figure 20, and the resulting particle displacements and rotations are shown in Figure 21.

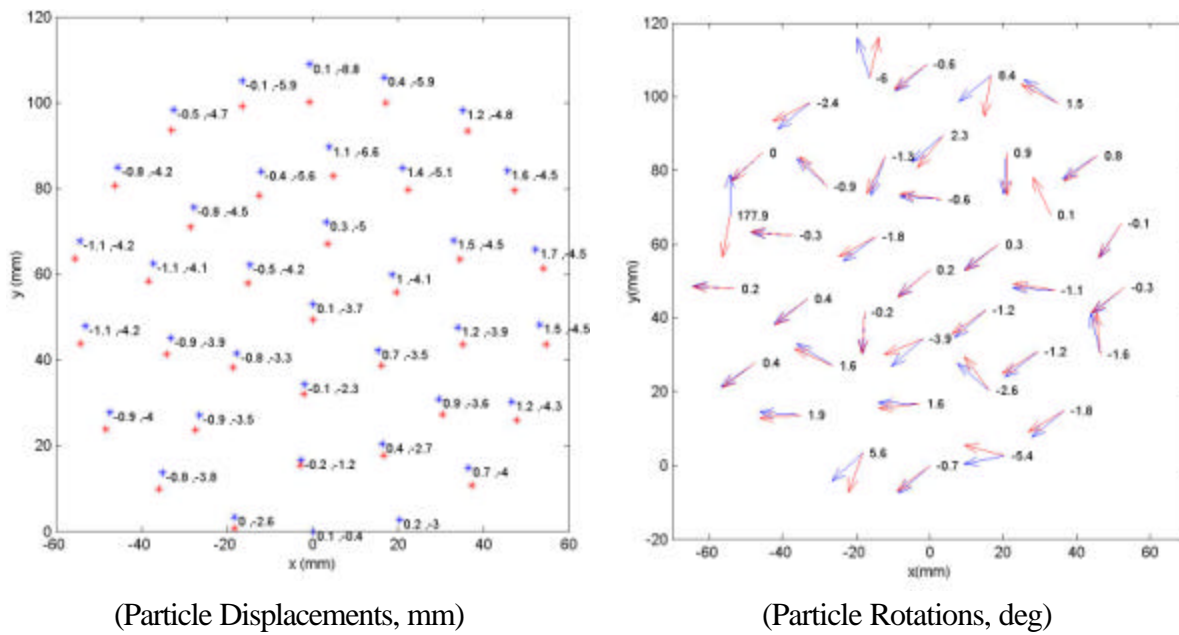


**FIGURE 21 Particle displacements and rotations for IDT specimen.**

Again using our finite element modeling code, a numerical simulation of this IDT test has been developed. For this case the experimental loading and displacement boundary conditions are more realistically simulated thereby providing a better comparison with the test. The generated model shown in Figure 22 has 37 particles with 92 binder elements. For this simulation, the element properties were modified to reflect the nature of the effective interparticle binder load transfer.

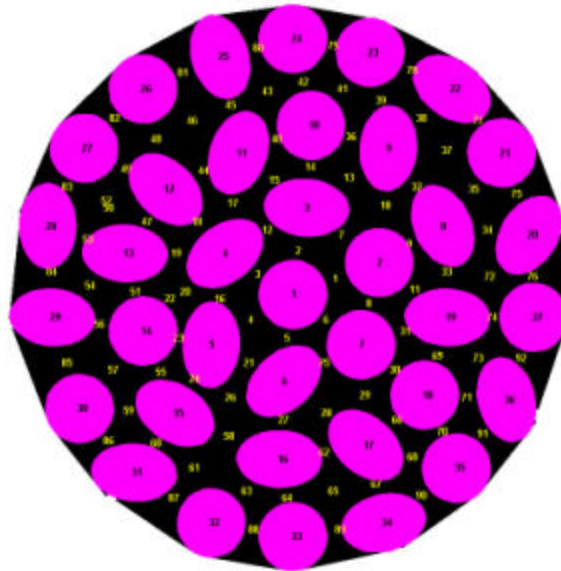


**FIGURE 22 Finite element model of IDT sample.**

Since the model was fully filled with polyurethane (binder cement), the element parameters were constructed using the fully-filled algorithm discussed in section 2.2.2. Furthermore since the exterior elements on the boundary of the circular specimen represent a less stiff effective medium, these elements had reduced elastic moduli in comparison to interior elements. The particular values used for each type of element were:  $E_{\text{interior}} = 5.2\text{MPa}$ ,  $\nu_{\text{interior}} = 0.48$ ,  $E_{\text{exterior}} = 4.5\text{MPa}$ ,  $\nu_{\text{exterior}} = 0.46$ . The three particles on the bottom of the model were held fixed to the

experimental data while the top particle was loaded with the experimental vertical load of 410N.

The model results of the particle displacements and rotations are given in Figures 23 and 24.

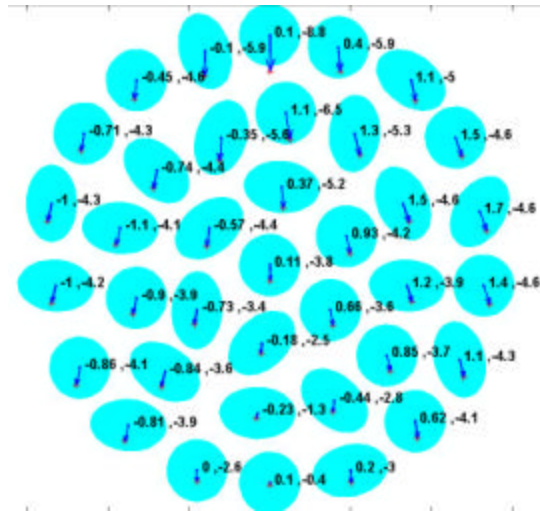


**FIGURE 23 IDT model results of particle displacements (mm).**

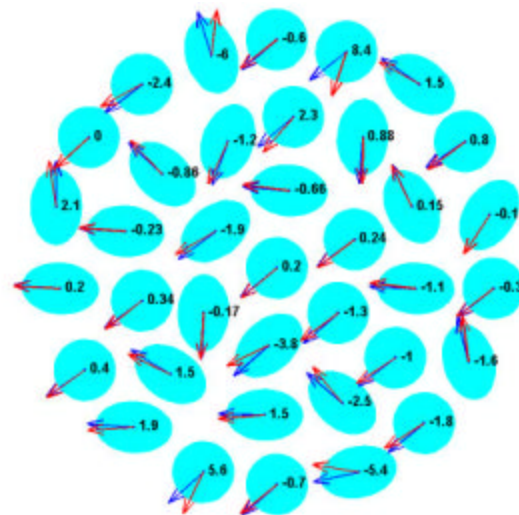


**FIGURE 24 IDT model results of particle rotations (deg, +ccw).**

The average error between the experimental data and the model predictions are given by the relations

$$\begin{aligned}
X_{error} &= \frac{\sum_{i=1}^{34} |X_i^{FEM} - X_i^{EXP}|}{\sum_{i=1}^{34} |X_i^{EXP}|} \times 100 = 5.9\% \\
Y_{error} &= \frac{\sum_{i=1}^{34} |Y_i^{FEM} - Y_i^{EXP}|}{\sum_{i=1}^{34} |Y_i^{EXP}|} \times 100 = 2.0\% \\
\theta_{error} &= \frac{\sum_{i=1}^{34} |\theta_i^{FEM} - \theta_i^{EXP}|}{\sum_{i=1}^{34} |\theta_i^{EXP}|} \times 100 = 4.9\%
\end{aligned} \tag{7}$$

Again the differences between the model predictions and the experimental data are generally within 5% thus indicating good agreement. Thus for the elastic case, the model appears to give verifiable results.

## 2.4 Indirect Tension Test Simulations

The indirect tension test (IDT) is commonly used to determine the tensile (splitting) strength, elastic modulus and Poisson's ratio of bituminous materials. Because of its wide use, this test has been chosen for our finite element simulations with the goal of trying to relate particular microstructure to observed test results.

### 2.4.1 General Simulation Procedures

The typical geometry of an IDT test is shown in Figure 25. A cylindrical specimen is loaded diametrically in compression, and this loading produces a somewhat uniform tension zone in the specimen across the loaded diameter. Normally the specimen thickness is to be kept smaller than the diameter, as per ASTM 4123. Because of uniform loading through the thickness, a two-dimensional circular cross-section may be taken for numerical simulation, as shown.

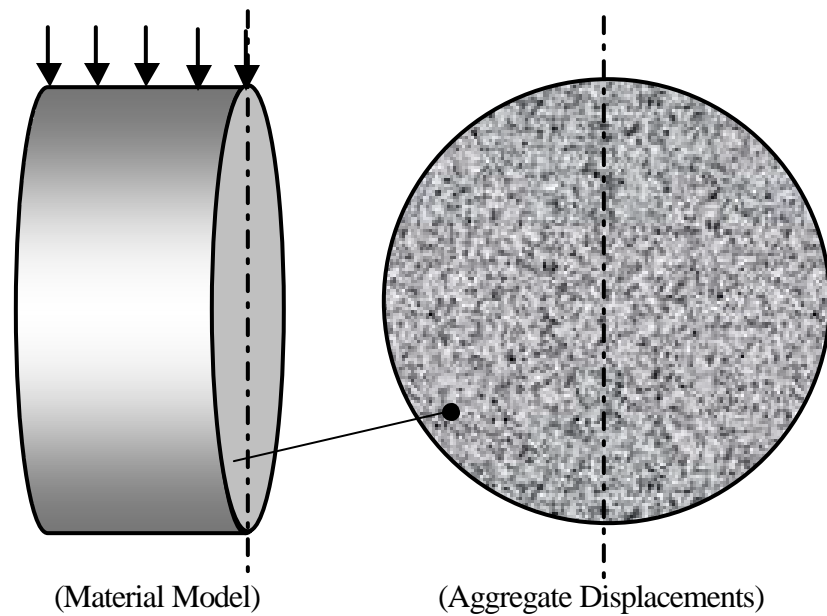


**FIGURE 25 Indirect tension test geometry.**

A simple numerical simulation of this test is shown in Figure 26. This model contains 64 circular particles and 167 elements. As shown in the figure, standard simulation output includes the aggregate displacement field and the internal interparticle force distribution between adjacent aggregates. Aggregate displacements are shown by scaled vectors indicating direction and magnitude, while the normal interparticle load transfer is shown by links whose line thickness indicates the relative magnitude of the force. As can be observed, the internal load distribution

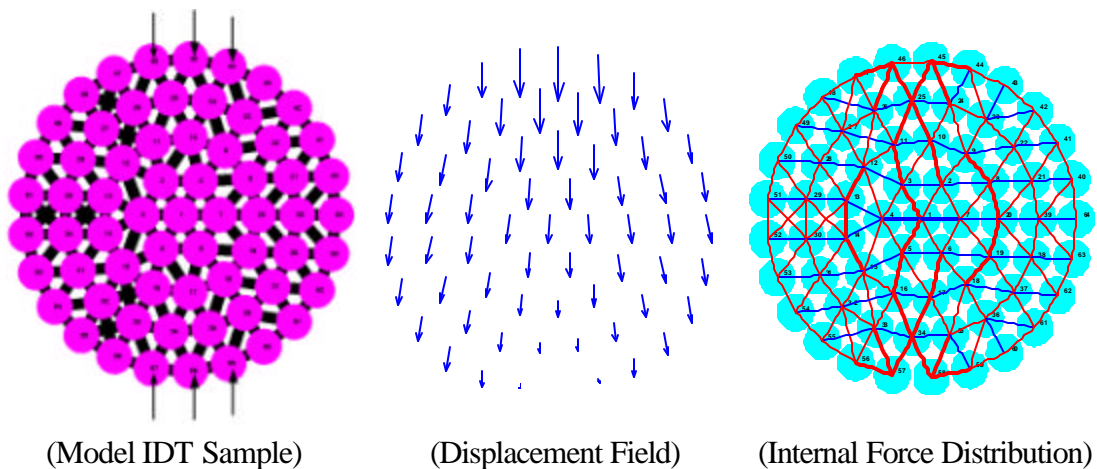


**FIGURE 26 Typical IDT simulation behavior.**

demonstrates vertical chains of compressive load transfer (red lines), and horizontal tension behavior (blue lines) in the central portion of the sample.

### 2.4.2 Variable Aggregate Models

In order to investigate some particular microstructural effects, two different variable aggregate IDT models have been created with different internal microstructure. Both model samples had a nominal diameter of 101mm (4in) and thickness of 70mm (2.75in), which are typical dimensions used in laboratory testing. Model 1 (shown in Figure 27) used a variable aggregate size distribution of 71 circular particles in groups of 14, 11, 7 and 4mm to approximate an actual sample gradation curve. Likewise model 2 (see Figure 28) had 96 particles from groups of 14, 11, 7, 4 and 2mm. These particle size distributions are compared with an actual sample gradation curve in Figure 29, and it is observed that Model 2 has a higher percentage of fine particles. Other model data is given in the Figures 27 and 28. Model boundary conditions constrain both horizontal and vertical displacements of the bottom aggregate(s), while the top particle(s) accept the applied vertical loading or displacement.

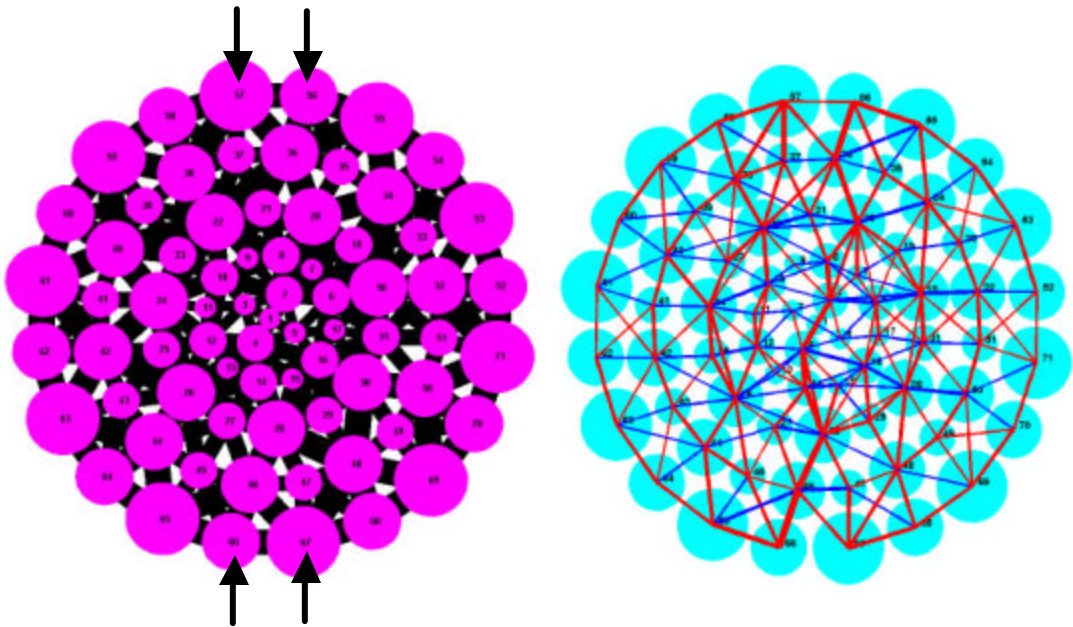


**FIGURE 27 IDT 71-particle (232 elements), variable mix model and internal force behavior.**

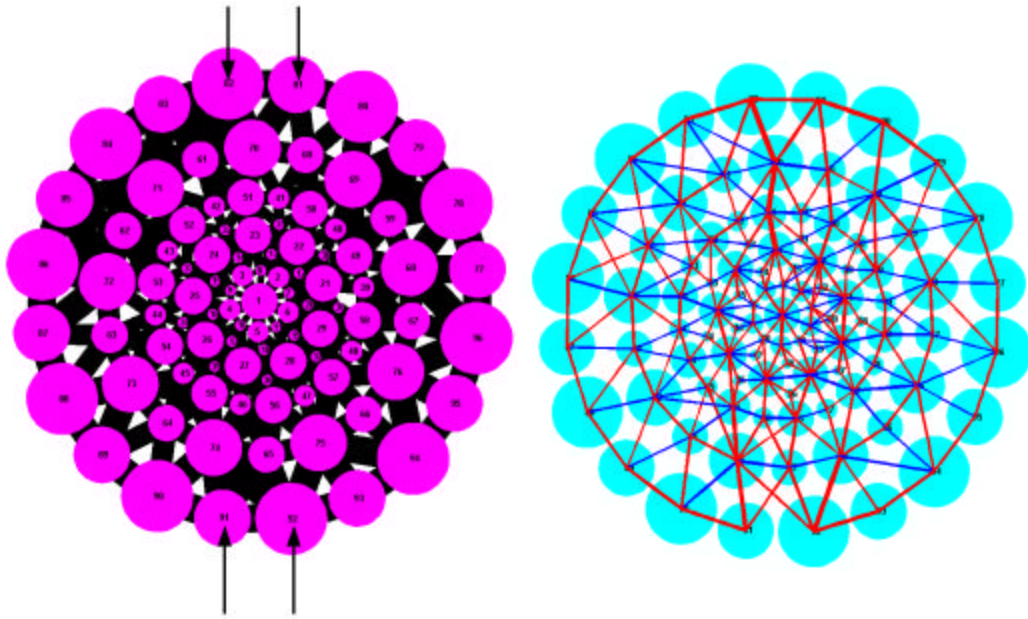


**FIGURE 28 IDT 96-particle (286 elements), variable mix model and internal force behavior.**

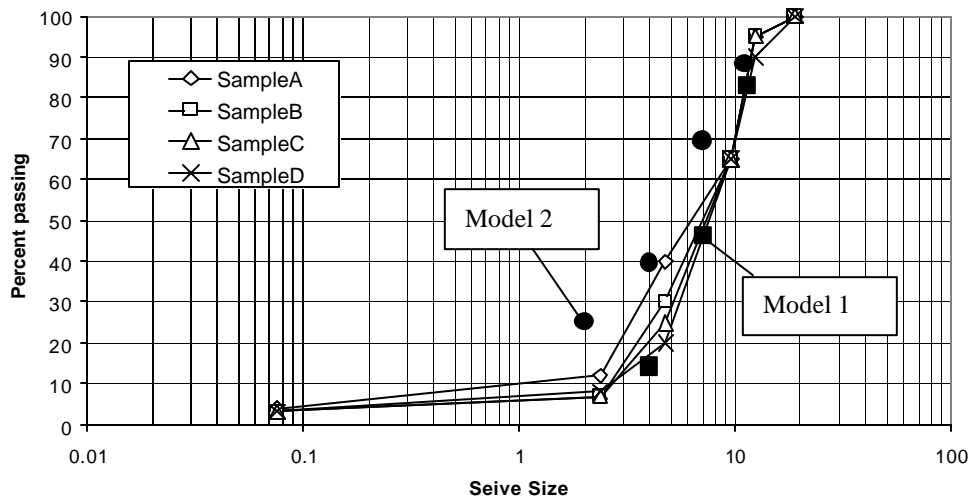


**FIGURE 29 Gradation comparison of IDT models with actual material.**

A series of numerical IDT simulations were conducted for each of these models using different values of binder moduli, and the results are shown in Figure 30. The variation of the binder properties was established from earlier studies by our research group using blends of

recycled asphalt (RAP) in sample mixes. The percentage of recycled product has been correlated with the initial elastic modulus, and the particular percentage-modulus values are given in the figure caption. For the case with identical binder properties, Model 2 gives slightly higher load-deflection sample stiffness when compared with Model 1. Thus as expected the finer material provides additional stiffening based on the added micromechanical network elements. Since the recycled material has higher stiffness, as the amount of included RAP material is increased, the overall specimen stiffness increases for each model.

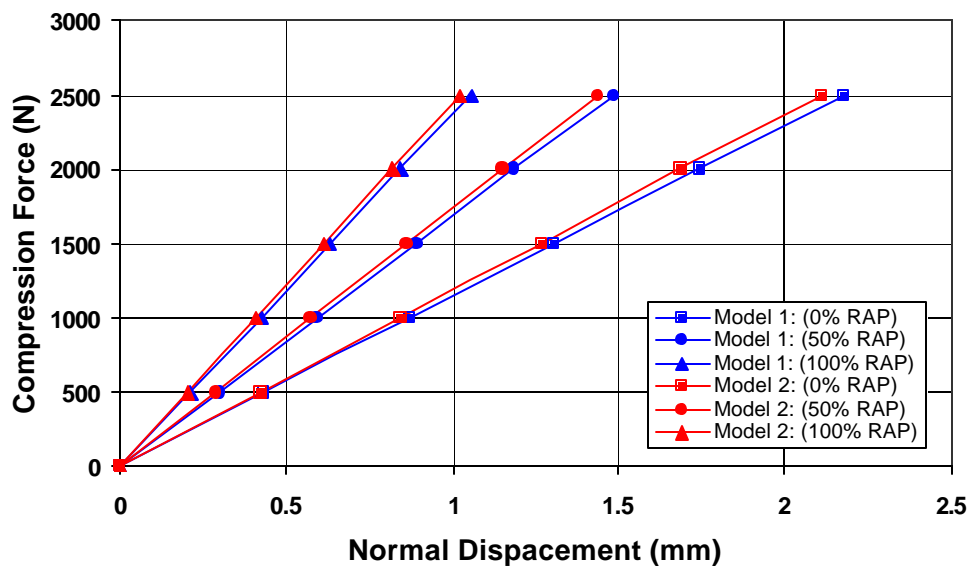


**FIGURE 30 Comparison of IDT models for different moduli/RAP content. (0% RAP,  $E = 0.47\text{MPa}$ ; 50% RAP,  $E = 0.64\text{MPa}$ ; 100% RAP,  $E = 0.98\text{MPa}$ )**

### 3. ABAQUS ASPHALT MODEL DEVELOPMENTS

In order to develop the modeling for nonlinear, inelastic asphalt behavior, use was made of the ABAQUS finite element software. ABAQUS is a general-purpose commercial code with many useful built-in features that include excellent nonlinear analysis methods and graphical pre- and post-processing. Another key feature in ABAQUS is its User Defined Subroutine in which the user can define custom elements for implementation and solution within the general code.

This feature would then allow our special microframe element defined in equation (2), to be incorporated within the ABAQUS code. Two different approaches using the ABAQUS package have been developed. The first approach used elasto-plastic, continuum elements originally given in the code. The second method incorporated our special microframe finite element within the user defined library.

### 3.1 Elasto-Plastic Continuum Model

#### 3.1.1 Basic Modeling Concept

The initial ABAQUS finite element modeling was developed using continuum two-noded rigid elements and four-noded quadrilateral elements. The general modeling scheme employed four-noded quadrilateral elements to simulate the binder material, and two-noded rigid elements to model the aggregate as shown in Figure 31. The rigid elements act to link the binder deformation with the aggregate rigid body motion and to transfer this behavior to the next neighboring aggregate. The particle center is the master node for the rigid aggregate and the other nodes on the perimeter have the same displacement as the center node. The master nodes have both displacements and rotations while the other perimeter nodes have only displacements.

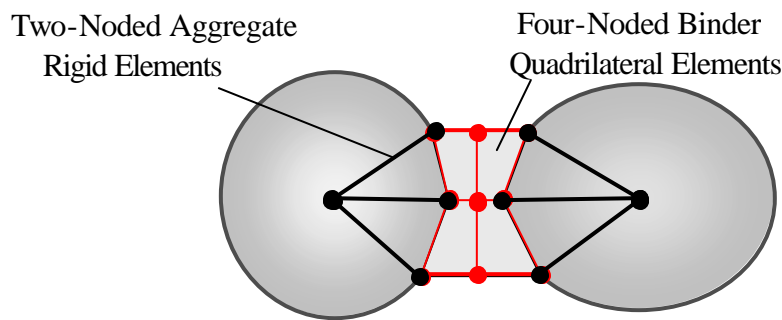


**FIGURE 31 ABAQUS modeling scheme.**

This modeling concept was used to develop a preliminary verification IDT model, which had seven particles as shown in Figure 32. Five different modeling approaches were used to

simulate the binder material. These schemes used one layer, one element; one layer, two element; two layer, four element; three layer, six element; and four layer, eight element models as shown. The binder material was distributed symmetrically with respect to the *branch vector* connecting neighboring particle mass centers. The uniform binder width was chosen to be 80% of the smaller particle radius perpendicular to the branch vector. The boundary binder node coordinates are calculated as the intersection of the binder boundary with the particle perimeter. For the multiple layer models, the binder layers are divided evenly along the branch vector. As before, model information including the nodal coordinates, element parameters and material properties are generated using our MATLAB code. This information is then incorporated into the input file for ABAQUS calculation.

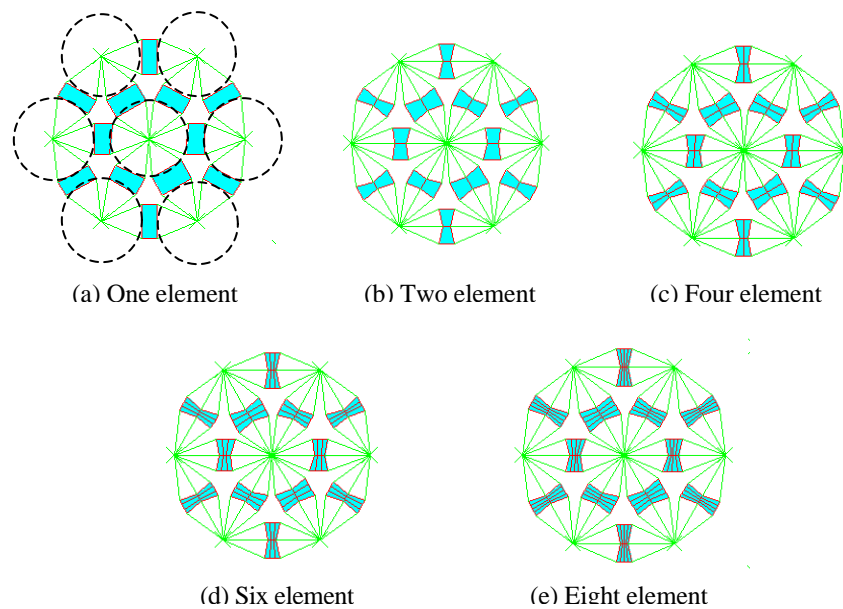


**FIGURE 32 Seven-particle IDT models**

Simulation results of the five IDT models in Figure 32 are compared in Figure 33. Sample compressive force is plotted versus the vertical deformation for each model. The one-element model uses the maximum thickness of the binder, and thus results in the lowest stiffness.

The two-element model mesh is very coarse and will not provide sufficient resolution of binder deformation. The results by using four elements (two layers), six elements (three layers) and eight elements (four layers) are almost identical, and thus appear to have adequate resolution of the binder deformation. Based on these results, the four element model was selected for future applications.

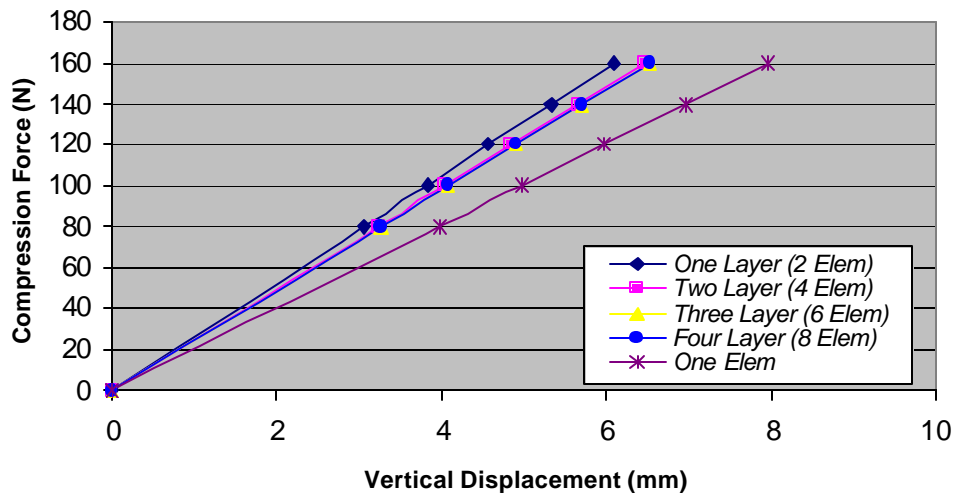


**FIGURE 33 FEM comparisons on the seven-particle IDT specimen.**

### 3.1.2. Elasto-Plastic Binder Properties

In order to determine the usefulness of the proposed ABAQUS modeling procedure, a more sophisticated two-dimensional IDT simulation was conducted. The model shown in Figure 34 has 65 particles, 195 binder areas and 7.6% porosity. This microgeometry results in a total of 780 deforming binder elements and 1170 rigid aggregate elements with connectivity as shown in Figure 35. Model boundary conditions impose compression forces on the particles 45 and 46 and fix the displacements on the particles 58 and 59.

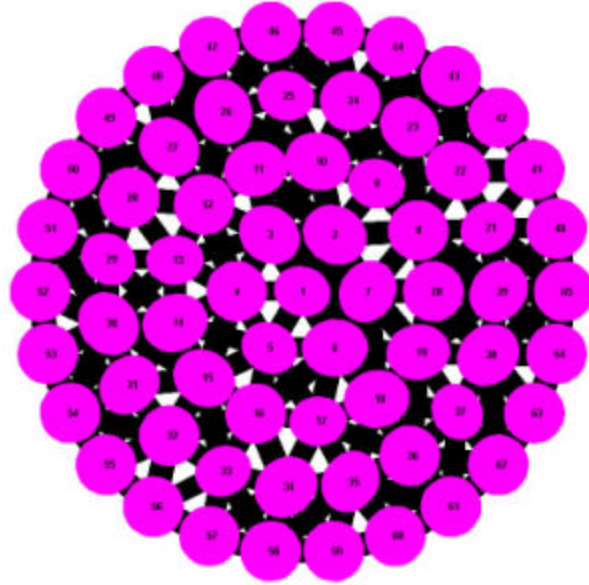


**FIGURE 34 IDT ABAQUS computational model.**

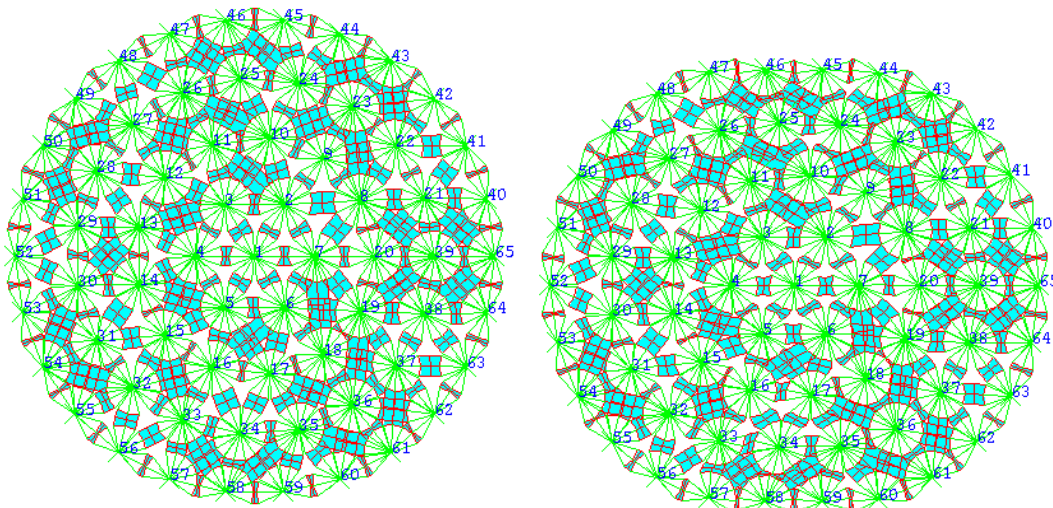


**FIGURE 35 Undeformed and deformed element meshes.**

The binder elements had elasto-plastic constitutive properties with nonlinear isotropic hardening behavior. The relationship between yield stress and equivalent plastic strain for the nonlinear plastic deformation is specified by

$$\sigma_{yield} = \sigma_0 + Q_\infty (1 - e^{-b\bar{\epsilon}_{pl}}) \quad (8)$$

where  $\sigma_0$  is initial yield stress,  $Q_\infty$  and  $b$  are nonlinear isotropic plastic constants to simulate the nonlinear hardening behavior. The quantity  $\sigma_0 + Q_\infty$  represents the maximum yielding stress for the binder material. Material parameters used for this model include elastic moduli  $E = 80$  MPa and  $\nu = 0.3$ ,  $\sigma_0 = 0.4$  Mpa,  $Q_\infty = 7.5$  Mpa and  $b = 12.5$ .

Displacement control was used for the simulation by imposing a vertical displacement (6 mm) to the top particles 45 and 46. Figure 36 illustrates the sample binder deformation in the  $x$  and  $y$  directions. The horizontal,  $x$ -displacements of the binder material increase from the vertical centerline to the sample boundaries, while the vertical  $y$ -displacements generally increase from bottom to the top. Particle displacement results from the rigid elements are shown in Figure 37, and it is observed that the particles move down and outward from the sample centerline. All of these plots are generated from the ABAQUS CAE Postprocessor Module.

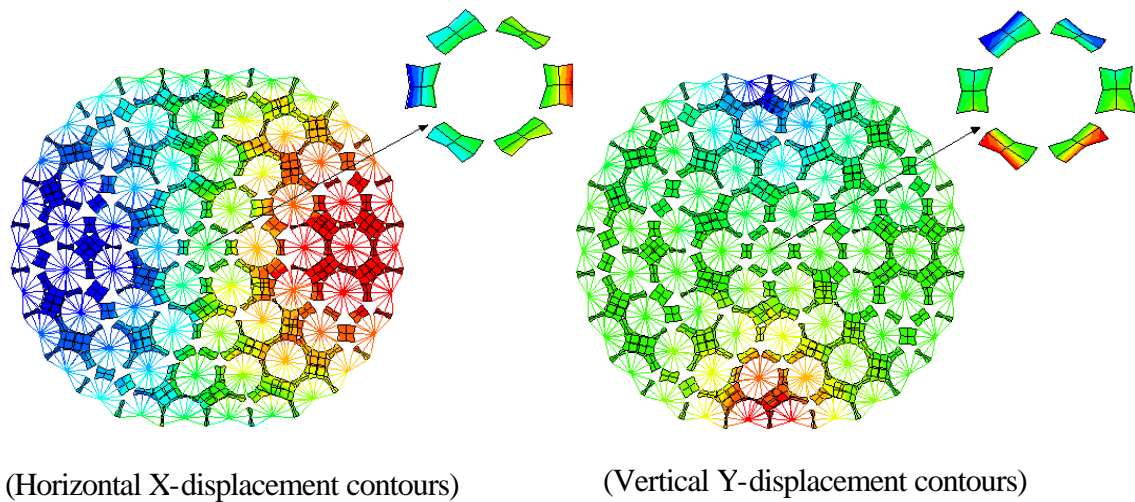


**FIGURE 36 Horizontal and vertical binder displacement contours.**



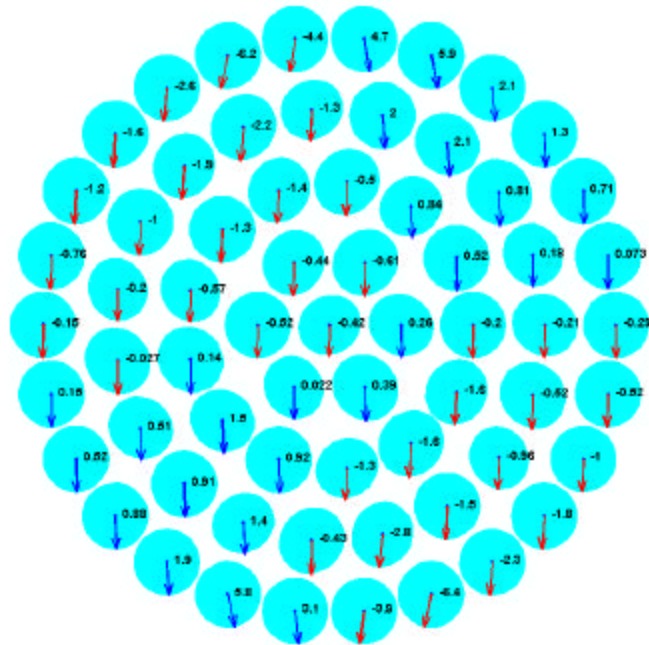


**FIGURE 39 Particle rotation distribution.**

ABAQUS stress distributions within the binder material for the IDT sample are shown in Figures 40 and 41. Figure 40 shows the von Mises stress contours while Figure 41 illustrates the horizontal normal component. The highest stresses generally occur along the sample's vertical centerline and decrease as one moves toward the boundary. Thus the central binder material has the largest tensile stress, thereby indicating that microcracking, damage and ultimate sample failure will initiate in this region.

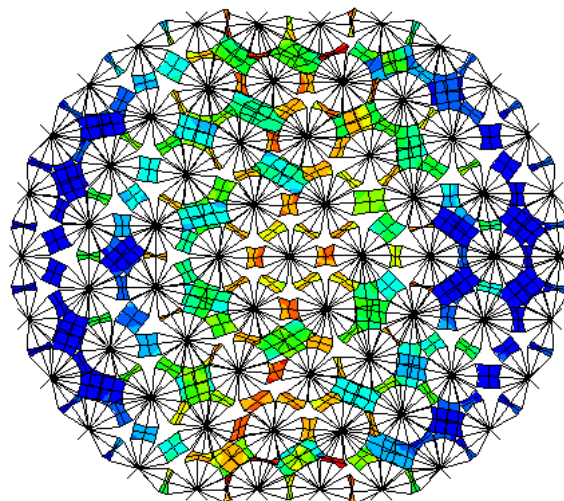


**FIGURE 40 Von Mises stress contours.**

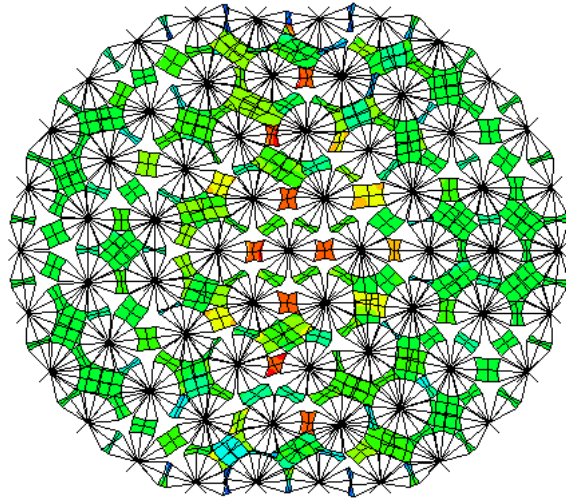


**FIGURE 41 Horizontal normal stress contours.**

The nonlinear elasto-plastic model response is shown in Figures 42 and 43. The relationship of yield stress to equivalent plastic strain for the nonlinear isotropic hardening behavior is shown in Figure 42 for a typical element response. The overall IDT sample vertical load versus vertical displacement is illustrated in Figure 43.

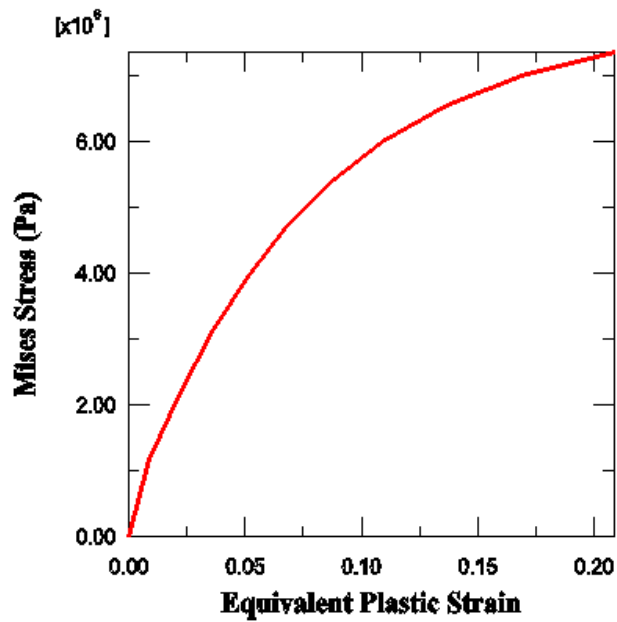


**FIGURE 42 Yield stress versus equivalent plastic strain.**

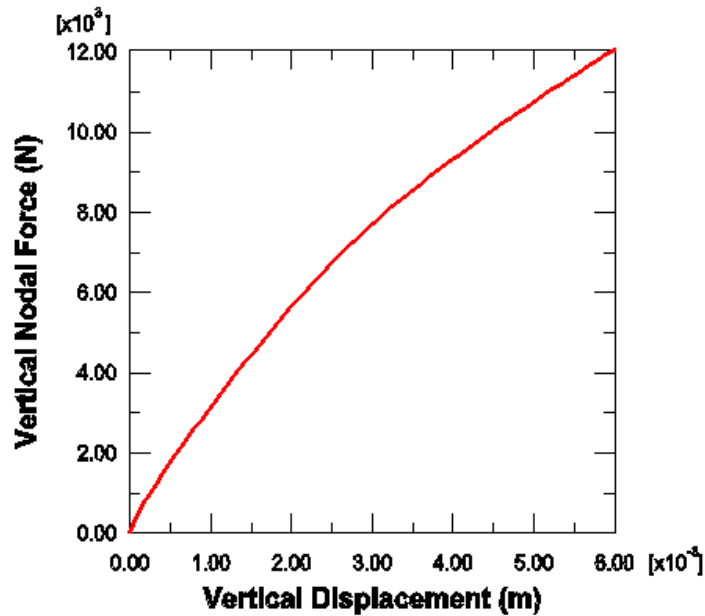


**FIGURE 43 Vertical force versus vertical displacement of IDT sample.**

It is observed that although this model may be able to simulate the nonlinear hardening behavior before sample failure, it cannot predict the nonlinear softening response after the maximum load point is reached. Based on this apparent limitation, a fundamental new modeling approach was initiated using our original micro-frame element incorporating a damage mechanics model to simulate softening behavior.

### **3.2 Microframe Model**

In order to simulate the significant softening behavior found in typical asphalt materials, we have incorporated a damage mechanics approach in our finite element modeling scheme. The particular method will use the micro-frame element model previously described in section 2 of this report. A damage mechanics theory will be used with this element, and this technique will provide the necessary softening behavior found in actual experimental data.

In order to use ABAQUS finite element software, we defined a user element (micro-frame element) to simulate the contact behavior between a pair of neighboring cemented particles. A User Subroutine was then developed to define the micro-frame element behavior, and this scheme then allows the use of the ABAQUS program to simulate IDT samples. Recall that these micro-frame elements were developed by analyzing the relationship of contact force and displacement between a pair of cemented particles, and this subroutine acts as the interface program to connect the ABAQUS software with the micro-frame elements.

### 3.2.1 Elastic Analysis and Verification with FEAMS Code

Initial work in the ABAQUS model development was to verify the linear user element subroutine by simulating an elastic example problem. The micro-frame element elastic matrix defined in the User Subroutine is the same as that used in the FEAMS code, see equation (2). We can therefore verify the elastic user element subroutine by comparing the ABAQUS simulation results with those from the FEAMS code on a common IDT model. Two verification simulations were conducted including a partial and full cemented model.

#### *Partial Cemented Model*

As shown in Figure 44, a partial cemented model was generated with 38 particles (from four different size groupings). This model had 111 elastic micro-frame elements with a sample porosity of 6%. For our use, porosity is defined in terms of volume measures as

$1 - (V_{aggregate} + V_{binder}) / V_{total}$ . The sample had a 83mm diameter and 100mm thickness. All binder material was symmetrically distributed with respect to each branch vector and had elastic moduli  $E = 1.0 \times 10^3$  psi and  $\nu = 0.3$ . To simulate IDT testing, the displacements of particle 33 and 34 were fixed and uniform compression forces were applied to particles 24 and 25 as shown in Figure 44.

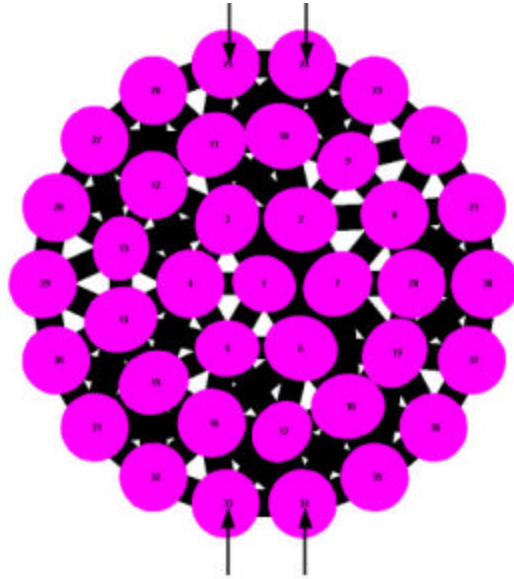


**FIGURE 44 Partial cemented verification model.**

Both the FEAMS and ABAQUS programs were used to simulate the elastic behavior of this model by increasing the compressive load from 2000 to 2800N. Simulation results of the particle displacements under the 2000N load are shown for each model in Figures 45 and 46. Comparison of these results indicates that the two models predicted nearly identical particle displacements.

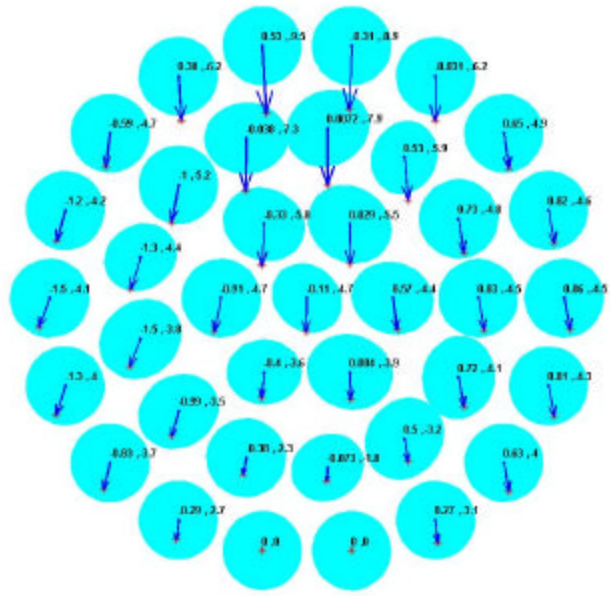


**FIGURE 45 Particle displacements (mm) – FEAMS results.**  
 . – Initial position      \* -- Current position

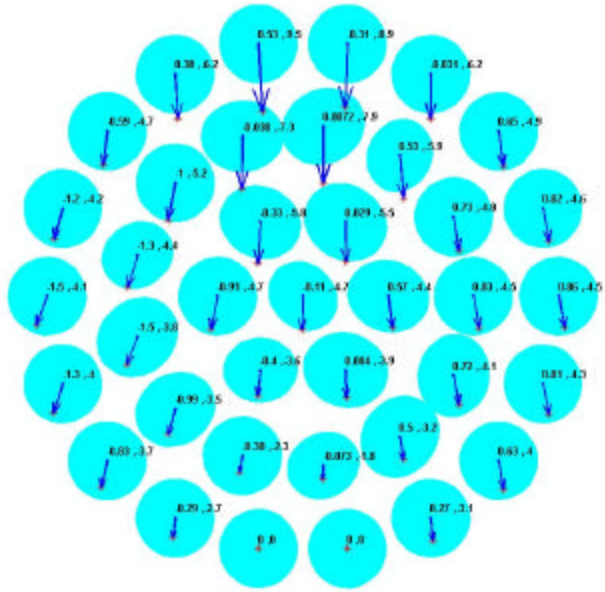


**FIGURE 46 Particle displacements (mm) – ABAQUS results.**  
 . – Initial position      \* -- Current position

The FEAMS and ABAQUS results are further compared during the load incrementation process in Figure 47. The overall compressive load versus vertical displacement is compared for each model. The linear elastic response for each case is almost identical.

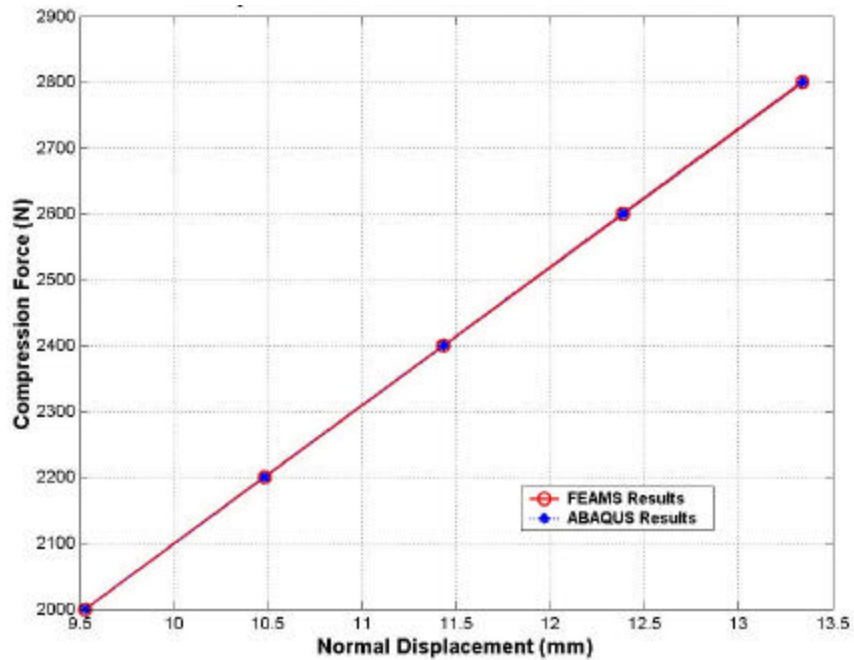


**FIGURE 47 Comparison of FEAMS and ABAQUS results.**

### *Full Cemented Model*

A second IDT verification model was developed for a fully cemented sample. While this model had the same number of particles and elements as the previous partial cement case, the binder fully filled the inter-particle region, see Figure 48. The binder elastic constants, sample dimensions and boundary conditions were the same as the previous case. Again the FEAMS and ABAQUS models were used to simulate this model by increasing the compressive load from 2000 to 2800N.

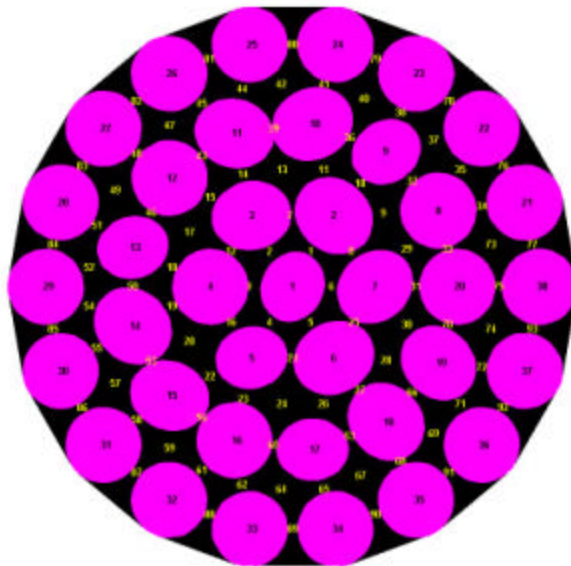


**FIGURE 48 Full cemented verification model.**

Figures 49 and 50 show the particle displacements under the 2000N loading. As before the predicted aggregate positions from each model are nearly identical.

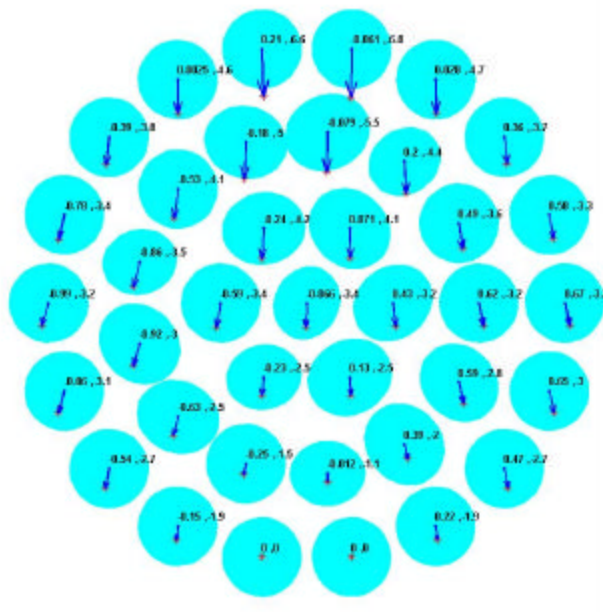


**FIGURE 49 Particle Displacements (mm) – FEAMS results**  
 . – Initial position      \* -- Current position

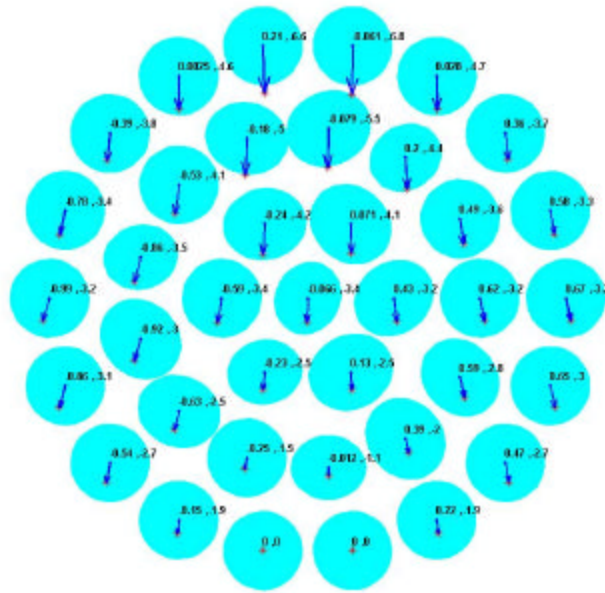


**FIGURE 50 Particle displacements (mm) – ABAQUS results.**  
 . – Initial position      \* -- Current position

Finally, FEAMS and ABAQUS simulation results of the overall sample load versus deformation are compared in Figure 51, and the results are again almost identical. Thus the ABAQUS verification for the elastic case appears to be adequate.

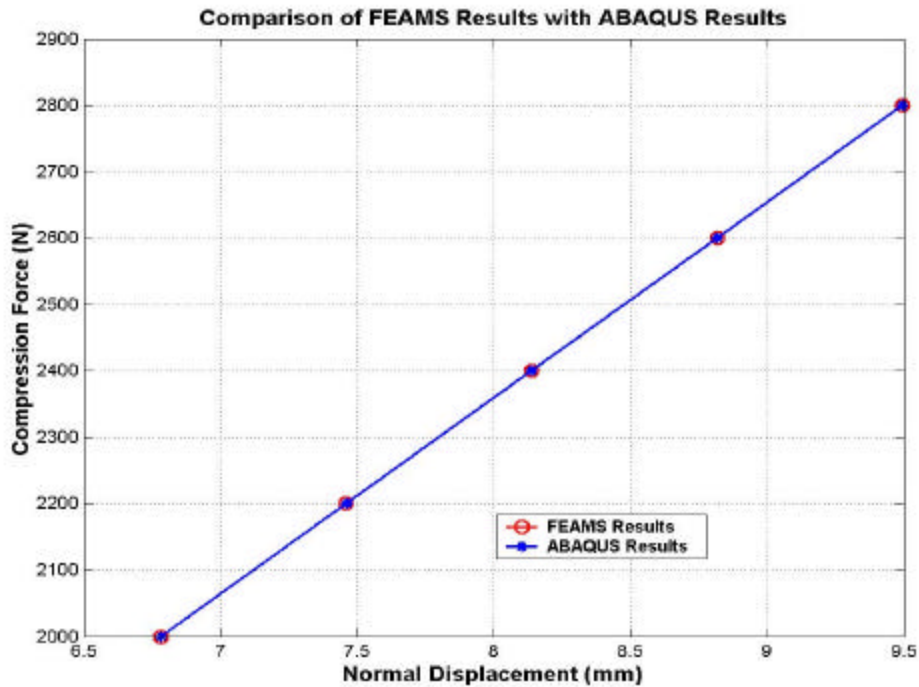


**FIGURE 51 Comparison of FEAMS an ABAQUS results.**

### 3.2.2 Inelastic Damage Model

Experimental IDT data has been collected on a series of asphalt samples prepared under Marshal mix design methods. The material had 30% recycled product, 5.4% total asphalt content (including RAP binder) and 6-8% air voids, and specimen dimensions were: diameter =105 mm and thickness = 64 mm. Additional details on the experimental program will be given in the next section. A typical failure pattern in the specimen during the softening response is shown in Figure 52. Cracking along the vertical diameter is clearly evident, and this behavior is thought to be the result of the coalescence of microcracks in the binder material and at the binder-aggregate interface. Specimen load-deflection data for four such IDT tests are illustrated in Figure 53. This data set shows the usual softening response after the peak strength has been

reached. Experimental observations of such behavior indicate that the strain softening may not be a material property of asphalt concrete treated as continua, but rather the performance of a microstructure composed of microcracks, joints and interfaces that results in an overall loss of strength. This concept leads to the desirability to have a micromechanical model which can incorporate damage behaviors in various microstructural components.



**FIGURE 52 IDT specimen showing sample failure.**

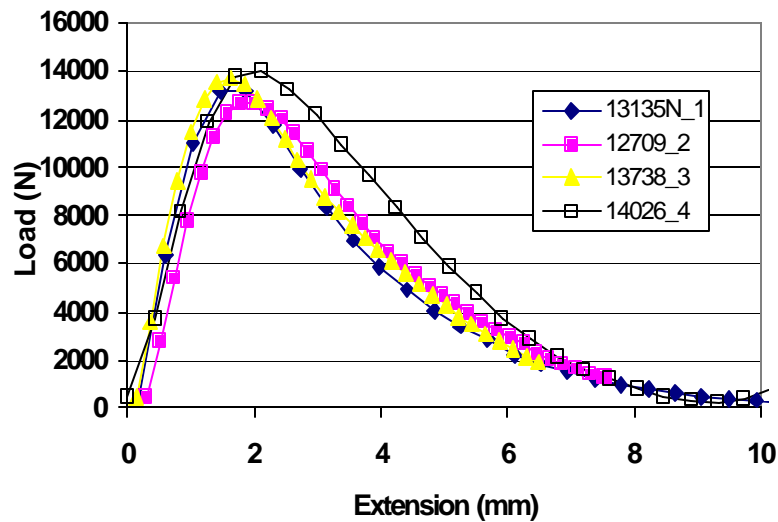


**FIGURE 53 IDT load deformation data.**

### *Damage Model Description*

In order to model the inelastic and softening behaviors observed in asphalt materials, a damage mechanics approach was coupled to the inter-particle cementation model. Previous work on damage model development has been previously reported by Zhong and Chang (42) for use with discrete element modeling. However, the approach by Ishikawa, Yoshikawa and Tanabe (43) was found to be more useful for our finite element model. The theory was originally developed for concrete materials whereby the internal micro-cracks within the matrix cement and around the aggregates are modeled as a continuous defect field. For our applications, the inelastic asphalt behavior is thus developed by the growth of damage within the binder material with increasing loading. A *damage tensor*  $[\Omega]$  is defined by considering the reduction of the effective area of load transfer within the binder continuum. The total strain field is defined as the sum of the elastic and damage strains

$$\{\boldsymbol{\varepsilon}\} = \{\boldsymbol{\varepsilon}_e\} + \{\boldsymbol{\varepsilon}_f\} \quad (9)$$

and thus the elastic constitutive relationship can be expressed as

$$\{\boldsymbol{\sigma}\} = [D_o]\{\boldsymbol{\varepsilon}_e\} = [D_o]\{\boldsymbol{\varepsilon} - \boldsymbol{\varepsilon}_f\} \quad (10)$$

where  $[D_o]$  is initial elastic stiffness matrix.

The damage strain represents the difference between the total and elastic strains and can be written as

$$\{\boldsymbol{\varepsilon}_f\} = \{\boldsymbol{\varepsilon}\} - \{\boldsymbol{\varepsilon}_e\} = [D_o]^{-1}[\Omega][D_o]\{\boldsymbol{\varepsilon}\} \quad (11)$$

This leads to the development of a damage stiffness matrix  $[D_s]$  defined by

$$\{\boldsymbol{\sigma}\} = ([I] - [\boldsymbol{\Omega}]][D_o]\{\boldsymbol{\varepsilon}\} = [D_s]\{\boldsymbol{\varepsilon}\} \quad (12)$$

Thus the damage stiffness matrix can be obtained from the initial elastic stiffness matrix

$$[D_s] = ([I] - [\boldsymbol{\Omega}]][D_o] \quad (13)$$

In order to characterize the particular damage behavior, consider the uniaxial case and choose an exponential model such that the hardening behavior is given as

$$\boldsymbol{\sigma} = f_c (1 - e^{-b(\boldsymbol{\varepsilon}/\boldsymbol{\varepsilon}_0)}) \Rightarrow \frac{\partial \boldsymbol{\sigma}}{\partial \boldsymbol{\varepsilon}} = D_o e^{-b(\boldsymbol{\varepsilon}/\boldsymbol{\varepsilon}_0)} \quad (14)$$

where  $f_c$  is the material strength,  $\boldsymbol{e}_0$  is the failure strain,  $b$  is the material parameter, and

$D_o = f_c b / \boldsymbol{\varepsilon}_0$  is the initial elastic stiffness. Using the damage stiffness definition from

relationship (13), the uniaxial damage stiffness  $D_s$  and the damage scalar  $\boldsymbol{\Omega}$  can be expressed as

$$D_s = (1 - \boldsymbol{\Omega}) D_o = D_o e^{-b(\boldsymbol{\varepsilon}/\boldsymbol{\varepsilon}_0)}, \text{ where } \boldsymbol{\Omega} = 1 - e^{-b(\boldsymbol{\varepsilon}/\boldsymbol{\varepsilon}_0)} \quad (15)$$

After maximum strength the softening behavior is taken as

$$\boldsymbol{s} = f_c (1 - e^{-b}) e^{m(1 - \boldsymbol{e}/\boldsymbol{e}_0)} \Rightarrow \frac{\partial \boldsymbol{s}}{\partial \boldsymbol{e}} = -\frac{D_o m}{b} (1 - e^{-b}) e^{m(1 - \boldsymbol{e}/\boldsymbol{e}_0)} \quad (16)$$

where  $m$  is the material parameter to be calibrated. The damage stiffness  $D_s$  and the damage

scalar  $\boldsymbol{\Omega}$  for the softening response become

$$D_s = (1 - \boldsymbol{\Omega}) D_o = -\frac{D_o m}{b} (1 - e^{-b}) e^{m(1 - \boldsymbol{e}/\boldsymbol{e}_0)}, \text{ where } \boldsymbol{\Omega} = 1 + \frac{m}{b} (1 - e^{-b}) e^{m(1 - \boldsymbol{e}/\boldsymbol{e}_0)} \quad (17)$$

The uniaxial stress-strain behavior corresponding to this particular constitutive model is shown in Figure 54 for the case of  $\epsilon_0 = 0.3$ ,  $b = 5$  and  $m = 1$ .

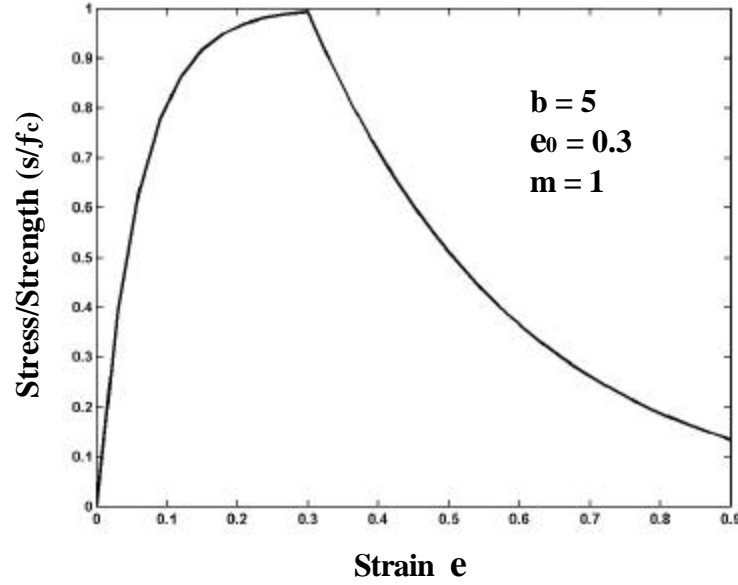


**FIGURE 54 Uniaxial stress-strain response for damage model.**

This damage modeling scheme was incorporated into the finite element network model by modifying the micro-frame element stiffness matrix given in equation (2). Using relation (15), the damage stiffness terms for the hardening behaviors can be written as

$$\left(K_{nn}\right)_s = K_{nn} e^{-b(\Delta u_n / \Delta U_n)}, \left(K_{tt}\right)_s = K_{tt} e^{-b(\Delta u_t / \Delta U_t)} \quad (18)$$

and using equation (17) the corresponding damage softening stiffnesses are given as

$$\begin{aligned} \left(K_{nn}\right)_s &= -(K_{nn} m / b)(1 - e^{-b}) e^{m(1 - \Delta u_n / \Delta U_n)} \\ \left(K_{tt}\right)_s &= -(K_{tt} m / b)(1 - e^{-b}) e^{m(1 - \Delta u_t / \Delta U_t)} \end{aligned} \quad (19)$$

where  $\Delta u_n$  and  $\Delta u_t$  are the normal and tangential accumulated relative displacements and  $\Delta U_n$  and  $\Delta U_t$  are the normal and tangential displacement failure criteria. Thus the element damage stiffness matrix  $[K_s]$  is found by replacing  $K_{nn}$  and  $K_{tt}$  with  $\left(K_{nn}\right)_s$  and  $\left(K_{tt}\right)_s$ .

The initiation of binder softening behavior for tension, compression and shear is governed by failure criteria based on accumulated relative displacements between particle pairs. A simple and convenient scheme to determine the failure criteria is based on using the dimensions of the inter-particle binder geometry in the form

$$\begin{aligned}\Delta U_n^{(t)} &= c_{nt} h_0 \\ \Delta U_n^{(c)} &= c_{nc} h_0 \\ \Delta U_t &= c_{tt} w\end{aligned}\tag{20}$$

where  $c_{nt}, c_{nc}, c_{tt}$  represent tension, compression and shear *failure factors*, which are constants that can be determined from experimental data and are expected to be in the range zero to one. Since the cementation geometry  $h_0$  and  $w$  will in general be different for each particle pair, it is expected that each element will have different failure criteria related to its local microstructure.

This damage-softening modeling scheme was incorporated in the ABAQUS finite element code using the nonlinear User Defined Element (UEL) subroutine. In the ABAQUS analysis, displacement control boundary conditions were employed and the Modified Riks method was used in order to provide a more stable solution scheme. Also, because aggregate (nodal) displacements became sizeable, the mesh geometry was updated during each load increment. Our MATLAB generator code created model geometry and provided model information files as an input for ABAQUS analysis.

### *IDT Simulation*

Preliminary IDT simulations of the inelastic softening behavior were conducted on the numerical sample shown in Figure 55. This model had a total of 65 particles in four particle size groupings: (5.2 mm x 4.5 mm), (6.0 mm x 5.2 mm), (5.8 mm x 5.0 mm) and (5.5 mm x 5.5 mm) and this resulted in 201 micro-frame elements as shown in Figure 56. The overall dimensions of the numerical sample were *diameter* = 105 mm and *thickness* = 63 mm, and these were approximately the same as the experimental specimen shown in Figure 52. Thus the numerical

results of this simulation can be compared with the experimental data shown in Figure 53. The boundary conditions used displacement control whereby the bottom pair of particles was fixed in both horizontal and vertical directions while the top particle pair was given prescribed incremental vertical displacements.

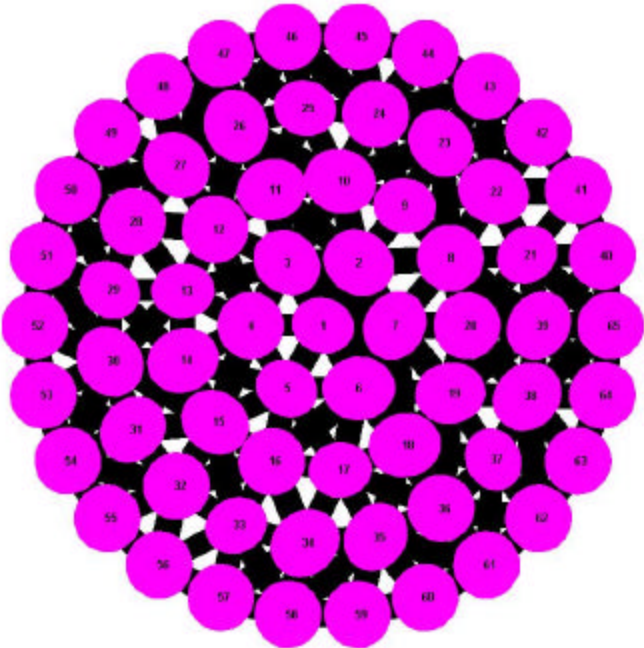


**FIGURE 55 IDT simulation model for damage case.**

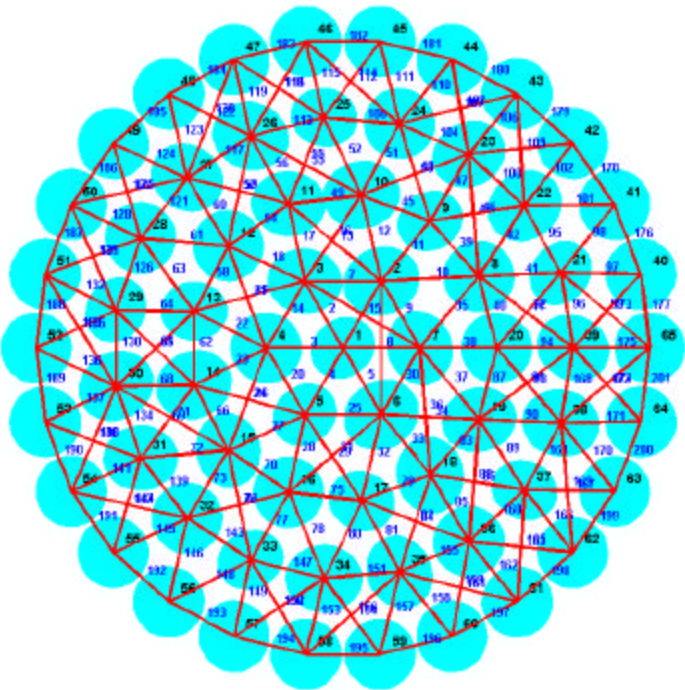


**FIGURE 56 Element mesh of model shown in figure 55.**

Two different simulations of this IDT sample were conducted. The first simulation (referred to as Model 1) used material parameters  $E = 130 \text{ Mpa}$ ,  $\mathbf{u} = 0.3$ ,  $b = 2$  and  $m=1$ , and was conducted under the case of a 10 mm vertical boundary displacement with failure factors of  $c_{nt} = 0.2$ ,  $c_{nc} = 0.2$ ,  $c_{tt} = 0.5$ . The second simulation (Model 2) had identical material parameters, but was loaded under 15 mm of vertical displacement with  $c_{nt} = 0.2$ ,  $c_{nc} = 0.33$ ,  $c_{tt} = 0.5$ . Simulation results of the sample vertical force versus displacement for each model are shown in Figure 57. Since each model had the same elastic and hardening parameters, the initial hardening responses of the two models are essentially identical. Model 1 with the lower value of element failure strain, goes into the softening regime sooner and thus gives less hardening behavior. In comparison, Model 2 provides more hardening behavior and thus develops a higher maximum load. With the chosen parameters, both models show similar softening response.

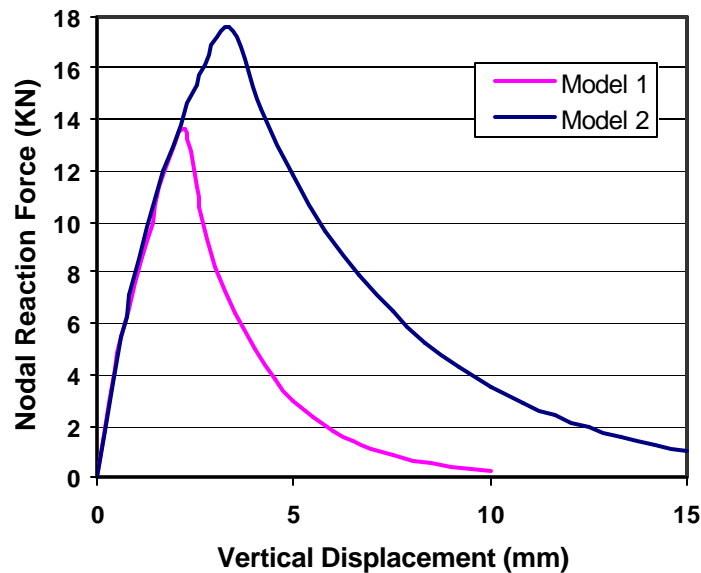


**FIGURE 57 Comparison of softening IDT models.**

Finally the numerical simulation results of Model 1 are compared with the experimental data set from Figure 53. This comparison is shown in Figure 58, and it is evident that the numerical results compare favorably with the experimental data. Thus it appears that the proposed damage model when incorporated with the micro-frame element can model the typical nonlinear hardening and softening response of IDT asphalt samples. Additional simulations are currently underway to investigate the model predictions for other variations in the model parameters.

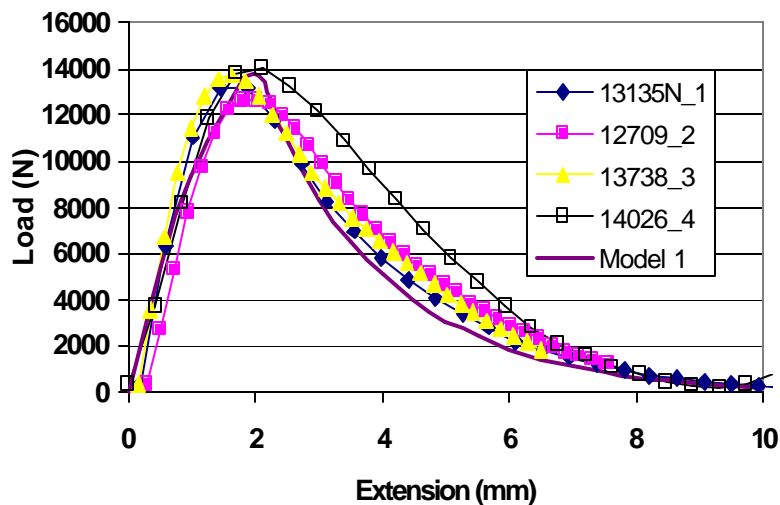


**FIGURE 58 Comparison of damage softening IDT model with test data.**

It should be pointed out that our experimental program (discussed in next section) investigated some properties of idealized binder material and determined an average compressive elastic modulus of about 83MPa. However, our choice of model parameters used  $E = 130\text{MPa}$ , and this selection along with several other parameters provided reasonably good agreement with the IDT data as shown in Figure 58. The lack of correspondence between the experimental modulus value and that used in the model can be explained. First the experimental binder

samples were idealized material made up from a single preliminary mix of fine material, mastic and recycled product. This mix was intended to approximate the actual material between the aggregates in the IDT samples. We feel that additional binder simulation mixes need to be investigated to determine a range of modulus values. Also, some parametric model studies need to be conducted in order determine the effect of different model parameters on the simulation results. Perhaps a lower modulus (more in keeping with the experimental value) could be used with a different set of the other model parameters. In any event, additional modeling and experimental work is needed to verify appropriate values of the model parameters, and such activities are planned.

#### **4. EXPERIMENTAL PROGRAM**

This research program also included a series of experimental studies on asphalt materials containing a fixed percentage of reclaimed asphalt produce (RAP). These studies included indirect tension tests and binder characterization experiments. Asphalt materials were collected from a local supplier, Cardi Construction Corporation in Warwick, Rhode Island. Collected material included sand and aggregates of nominal size 19 mm (3/4 inch), 12 mm (1/2 inch) and 9 mm (3/8 inch). Collected reclaimed asphalt product included processed material having nominal size 19 mm (3/4 inch) and 9 mm (3/8 inch) in the “as received” condition. The aggregates and sand were dried to remove the moisture content and sieved to determine their individual gradation. The gradations of each of these stocks are shown in Figure 59. The asphalt content of the reclaimed product was determined to be 4.6 % by the ignition method as per ASTM. D6307-98. The RAP was also sieved to establish size gradation.

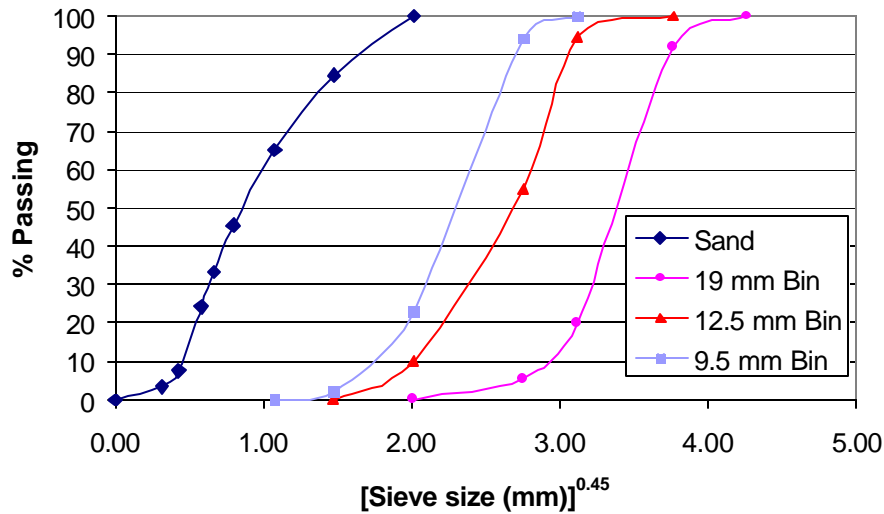


**FIGURE 59 Size gradation of virgin aggregates and sand.**

#### 4.1 Indirect Tension Testing

Indirect tension test samples of size 105 mm diameter and 64 mm height were prepared following the Marshall design procedures. The mix gradation is shown in Figure 60 and included 30% RAP content. A series of test samples were first prepared by varying the total asphalt content from 4.9 % to 5.9 % in steps of 0.5 %. Marshall stability, Voids in Total Mix (VTM) and Marshall flow were then evaluated. From these tests and using the RIDOT specification for binder course, the optimum asphalt content was determined to be 5.4 %. Subsequent samples for indirect tensile testing were prepared with 5.4 % total asphalt content following the Marshall compaction method. The amount of virgin asphalt to be added was determined by discounting the estimated asphalt binder in the RAP from the total asphalt content of 5.4%.

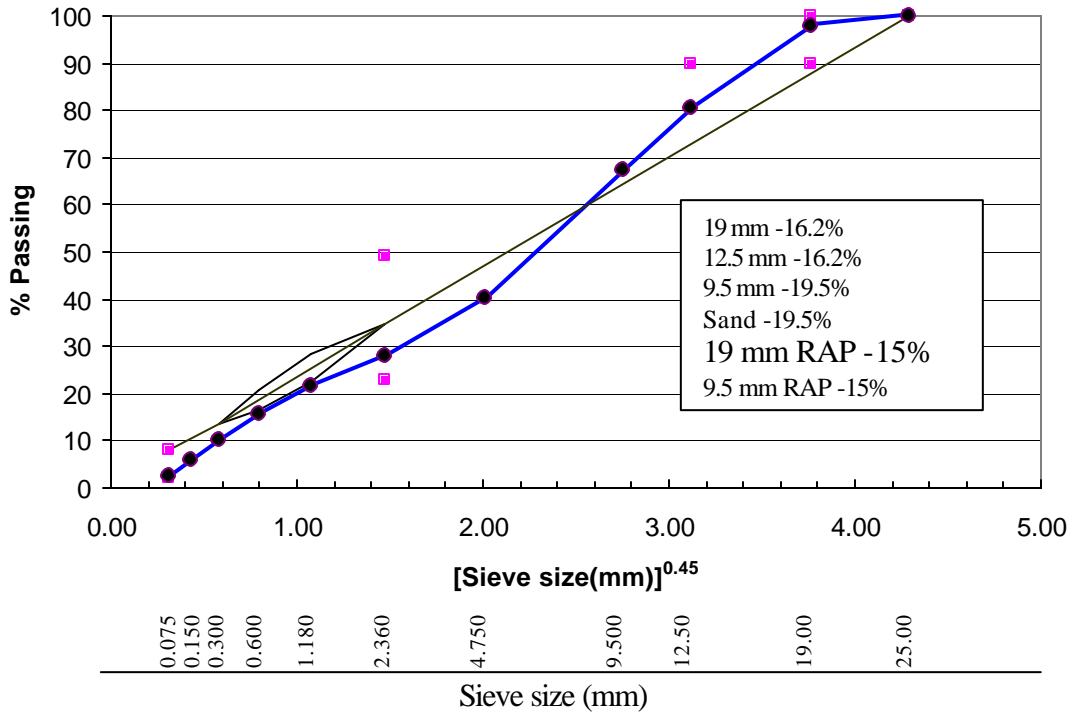


**FIGURE 60 Marshall mix design for IDT test samples with 30% RAP.**

The prepared specimens were tested under diametrical compression in an Instron testing system at a loading rate of 50mm/minute. A transducer fixture was constructed in order to record the lateral expansion of the specimen, and the test set up is shown in Figure 61. The vertical loading and sample vertical and lateral deformation were recorded continuously.



**FIGURE 61 Loading fixture for indirect tensile testing.**

From this data, the splitting strength of the specimen  $\sigma_s$  was calculated using the well-known relationship

$$\sigma_s = \frac{2P}{\pi DL} \quad (21)$$

where P is the maximum load, and D and L are the sample's diameter and length, respectively. Load-load point displacement response from four different tests are shown in Figure 62, and the lateral expansion versus load-point displacement are shown in Figure 63. The average splitting strength was obtained as  $1.32 \pm 0.095$  MPa.

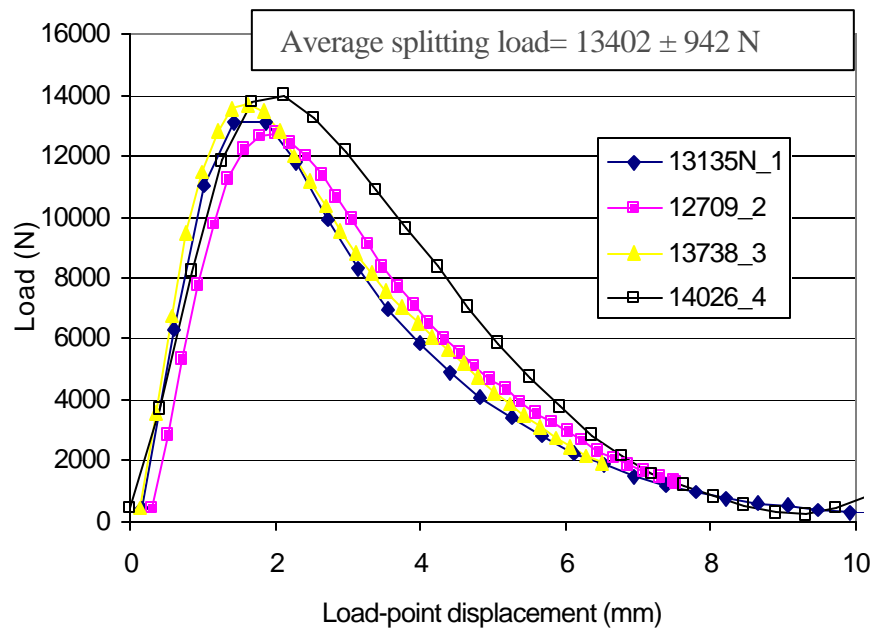


**FIGURE 62 Load versus load-point displacement response for indirect tensile tests.**

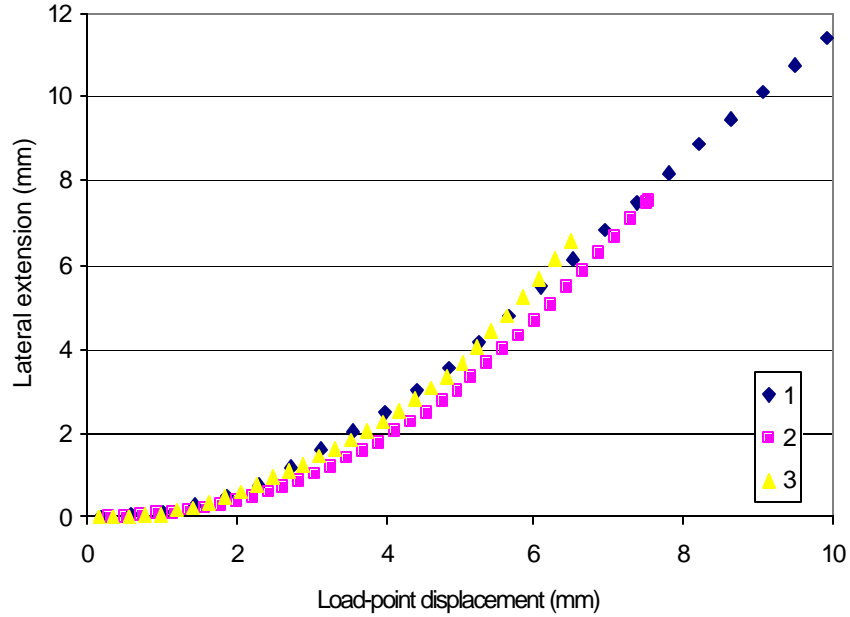


**FIGURE 63 Lateral extension versus load-point displacement for three indirect tensile tests.**

#### 4.2 Visualization of Damage Evolution During IDT Tests

During an indirect tension test, the specimen fails by splitting along the diameter in line with the loading direction. This behavior is associated with the evolution of damage (micro-cracking) and the subsequent growth of damage leading to sample failure. In order to visualize this behavior in real-time, an IDT specimen was photographed using a digital camera at a speed of 1.6 frames/sec. The temporal sequence of this event as recorded along with the instantaneous load is shown in Figure 64. The time sequence shown is from left to right in each row, and the instantaneous load (lb) can also be seen in each of the photographs. It can be observed from this figure that no visible damage is seen until the load reaches the maximum sample load of 4396 lb (19.5kN). The first sign of noticeable damage (cracking) is seen in the next photograph corresponding to a load of 3993 lbs near the top-loading strip. This damage progresses downward as the loading continues, meets with the cracks initiated near the bottom loading strip and eventually splits the specimen along the loading diameter. Our subsequent efforts are to slice

the face of the sample, exposing the aggregate morphology and track the displacement and rotation of individual aggregates in real-time during the splitting test.

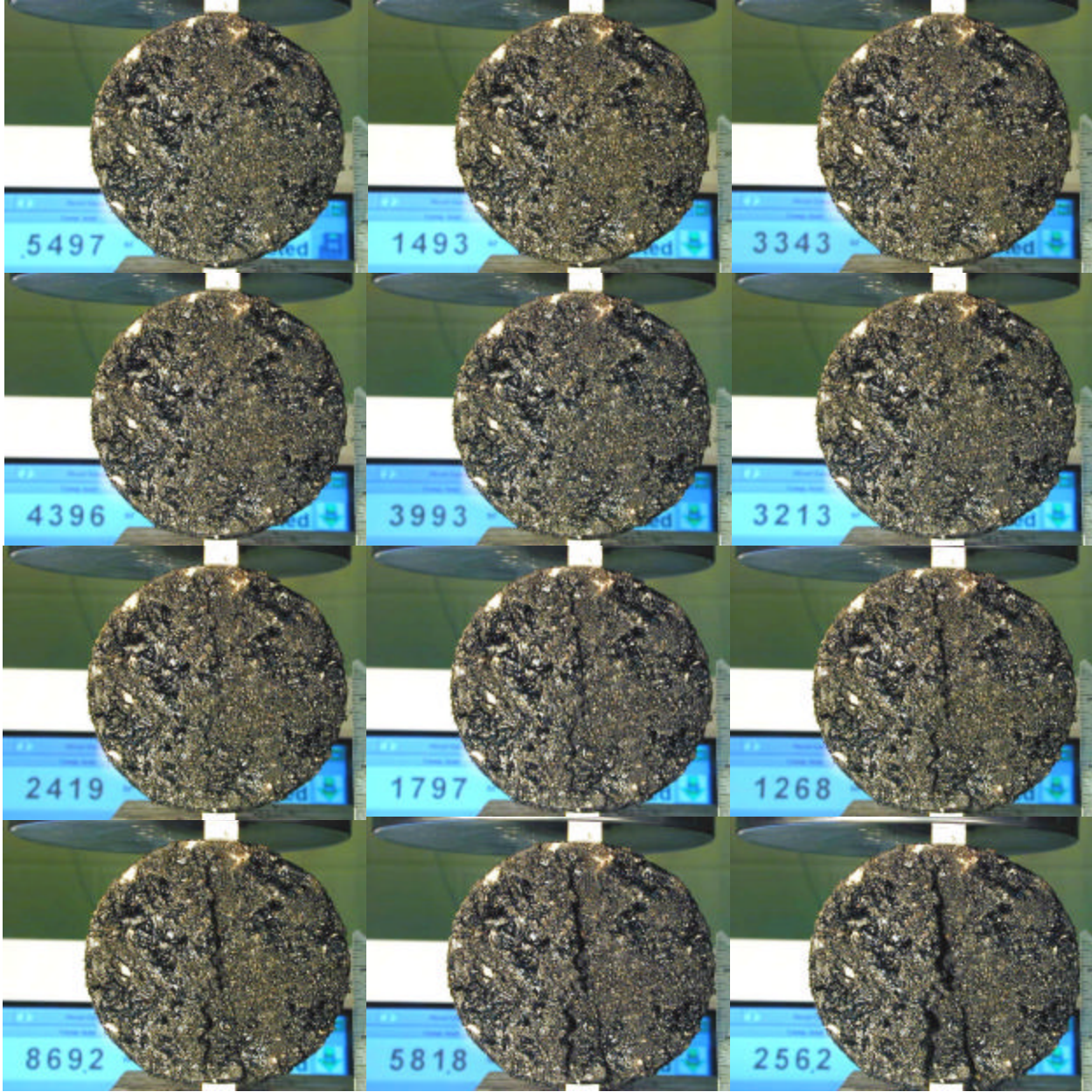


**FIGURE 64** Real-time damage evolution and failure during an indirect tension test. Photographs are time sequenced from left to right in each row.

### 4.3 Characterization of Binder Strength and Stiffness

The numerical model incorporating damage to simulate asphalt softening behavior requires knowledge of the binder characteristics. The binder is taken to be the material between the asphalt aggregates, and this would include the mastic, additives (if any), and the fine material with particle size less than a millimeter. Thus the binder consists primarily of asphalt and fine aggregates in the size range of 0.075-0.6 mm, which corresponds to a sieve size of 200-30.

In order to investigate the tensile and compressive behavior of the binder material, special cylindrical samples were prepared. The samples were 44mm in diameter and 50mm high, and were made using mastic and fine aggregates in the range 0.075-0.6 mm. In preparing these samples, both RAP and new material were sieved to collect the fines (0.075-0.6mm). The RAP was then mixed with new material in proper proportion to produce a binder sample with 30% RAP and 5.4% overall asphalt content. This mix was then identical to the parameters used in the indirect test samples. Following the procedures of Kennedy, et al. (41), a constant compaction pressure of 6200 lb was applied for 20 minutes at 275<sup>0</sup> F, after placing the mix in the mold. The samples were then tested in compression and indirect tension at a loading rate of 2.5 mm/minute. Figure 65 shows the compression stress-strain behavior for three binder samples. It can be observed that the behavior is approximately linear up to the maximum stress. The average compressive modulus was 83 MPa and the average compressive strength was 2.3 MPa.

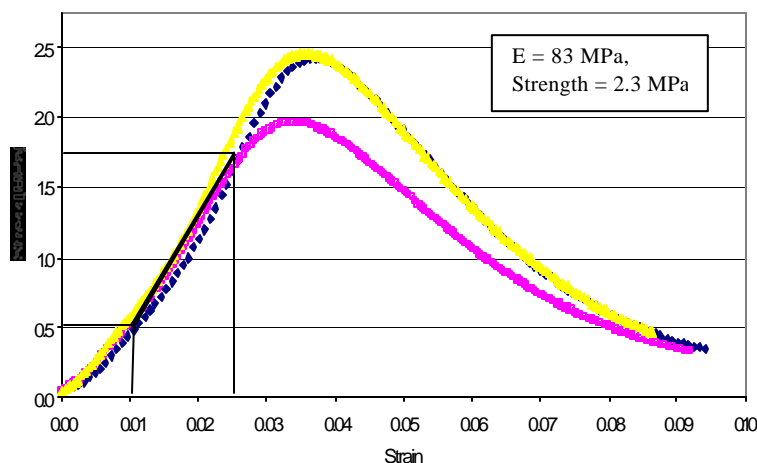


**FIGURE 65 Compressive stress-strain behavior for asphalt binder.**

The binder samples were also used as an indirect tension specimen. Load versus load-point displacement data for three indirect tensile tests are shown in Figure 66. The average splitting strength was found to be 0.38 MPa.

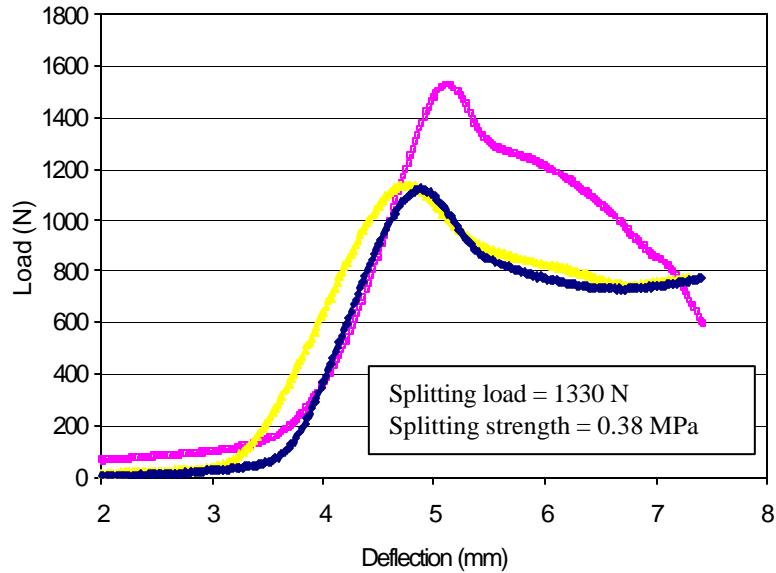


**FIGURE 66 Load versus load-point displacement response for indirect tensile test of asphalt binder elements.**

It should be pointed out that these binder characterization results are preliminary, and additional testing with other mix parameters are needed to verify these values.

## 5. SUMMARY & CONCLUSIONS

This study has developed a new micromechanical numerical model for asphalt materials. The model is based on microstructural simulation and incorporates nonlinear inelastic behavior through the use of damage mechanics. Asphalt microstructure was incorporated into the model by replacing the aggregate-binder system with an equivalent two-dimensional finite element network that represents the load-carrying behavior between aggregates in the multiphase material. These network elements were specially developed from an elasticity solution for cemented particles. Incorporating a damage mechanics approach with this solution, allowed the

development of a softening model capable of predicting typical global inelastic behaviors found in asphalt materials. This theory was then implemented within the *ABAQUS* FEA code using the User Defined Element subroutine. The modeling also developed a material generating computer code, which was used to create idealized asphalt with aggregate-binder systems exhibiting varying degrees of microstructure.

Experimental verification studies were conducted on specially prepared cemented particulate systems including a compression sheet and an indirect tension sample. These experiments allowed detailed measurement of aggregate displacements and rotations using video imaging and computer analysis. Model simulations of these tests gave results that compared favorably (1.5-7%) with the experimental data. Further experimental work included indirect tension testing and damage visualization studies on IDT samples. Preliminary experimental characterization of idealized binder material was also conducted for both compressive and tensile properties.

IDT simulations were made on samples with various microstructures and material properties. A pair of identical global size samples was created with different aggregate gradation. Load-deflection behaviors of these two samples were compared to demonstrate the gradation-microstructural effect, and results indicated that the sample with the higher percentage of fine aggregate had a slightly higher stiffness. Simulations of these two samples with variation of the binder moduli was also conducted. Values of the binder moduli were determined from previous work on recycled asphalt material (RAP), and the higher percentage of RAP corresponded to stiffer binder moduli. The model predictions indicated a stiffer load-deflection response with higher binder moduli.

Preliminary inelastic IDT simulations were conducted using the damage mechanics model. Two simulations were made with displacement boundary control for samples with

different micro-failure strains. The sample with the higher failure strain had more hardening behavior and gave a higher maximum load before global specimen failure. As reported in previously published work, strains in the binder are considerably larger than the overall macroscopic strain in the IDT sample. Comparison of these simulations with experimental data indicated a reasonable match, but further studies of this inelastic behavior are needed to justify the particular softening model.

Additional simulations are currently underway to investigate the effects of microstructure (fabric) and binder material parameters on the numerical predictions. We also wish to establish where damage initiates and its subsequent evolution within a test sample. Future experimental work will include IDT, binder and fracture testing. We also intend to experimentally investigate more details on aggregate displacements and rotations and binder damage behavior during the inelastic-softening response.

## **6. ACKNOWLEDGEMENT**

The authors would like to acknowledge supported from the Transportation Center at the University of Rhode Island under Grant 00-38. Additional support was also provided from the Northeast Asphalt Institute and Cardi Construction Corporation.

## **7. REFERENCES**

- (1) Schimmoller, V.E, Holtz, K, et.al., Recycled Materials in European Highway Environments: Uses, Technologies and Policies, FHWA/US DOT Report, Presented at 80<sup>th</sup> TRB Meeting, Washington, D.C., January, 2001.
- (2) Kandhal, P.S., Rao, S.S., Watson, D.E. and B. Young, Performance of Recycled Hot Mix Asphalt Mixtures”, NCAT Report No. 95-1, 1995.

- (3) Brayton, T.E., Lee, K.W., Gress, D. and J. Harrington, Development of Performance-Based Mix Design for Cold In-Place Recycling of Asphalt Mixtures, Proc.80<sup>th</sup> Transportation Research Board Meeting, Washington, D.C., 2001.
- (4) Salam, Y.M. and C.L. Monismith, Fracture Characteristics of Asphalt Concrete, Proceedings of the Association of Asphalt Paving Technologists (AAPT), Vol. 41, 1972.
- (5) Majidzadeh, K. and Kauffmann, E., Verification of Fracture Mechanics Concepts to Predict Cracking of Flexible Pavements, Research Foundation, Ohio State University, RF 3200, Final Report, 1973.
- (6) Majidzadeh, K., Dat, M. and F. Makdisi-Ilyas, Application of Fracture Mechanics for Improved Design of Bituminous Concrete, Report No: FHWA-RD-76-92, 1976.
- (7) Karakouzian, M. and K. Majidzadeh, Practical Method for Evaluating Fatigue and Fracture Toughness of Paving Materials, AAPT Proceedings, 1978.
- (8) Sousa, J. and C.L. Monismith, Dynamic Properties of Asphalt Concrete, Journal of Testing and Evaluation, Vol. 114, No: 4, 1988.
- (9) Tschegg, E.K, Kroyer, G., Tan, D.M, Stanzl-Tschegg, S.E., and J. Litzka, Investigation of Bonding Between Asphalt Layer on Road Construction, J. Transportation Eng., Vol. 121, pp. 309-316, 1995.
- (10) Mobasher, B., Mamlouk, M.S., and H.M. Lin, Evaluation of Crack Propagation Properties of Asphalt Mixtures, J. Transportation Eng., Vol. 123, pp. 404-413, 1997.
- (11) Sulaiman, F. J. and A.F. Stock, The Use of Fracture Mechanics for the Evaluation of Asphalt Mixes, AAPT Proceedings, Vol. 64, 1996.
- (12) Venkatram, S., Fracture Toughness and Dynamic Constitutive Characterization of Recycled Asphalt Pavement Binder, Masters Thesis, University of Rhode Island, 1996.

- (13) Dvorkin, J., Nur, A., H. Yin, Effective Properties of Cemented Granular Materials, Mech.of Materials, Vol 18, pp 351-366, 1994.
- (14) Zhu, H., Chang, C.S. and J.W. Rish, Normal and Tangential Compliance for Conforming Binder Contact I: Elastic Binder, Intl. J. Solids Structures, Vol. 33, pp 4337-4349, 1996.
- (15) Zhu, H., Chang, C.S. and J.W. Rish, Normal and Tangential Compliance for Conforming Binder Contact II: Viscoelastic Binder, Intl. J. Solids Structures, Vol. 33, pp 4351-4363, 1996.
- (16) Chang, C.S. and J. Gao, Rheological Modeling of Randomly Packed Granules With Viso-Elastic Binders of Maxwell Type, Comp. and Geotech., Vol. 21, pp. 41-63, 1997.
- (17) Cheung, C.Y., Cocks, A.C.F. and D. Cebon, Isolated Contact Model of an Idealized Asphalt Mix, Intl. J. Mech. Sci.,Vol. 41, pp. 767-792, 1999.
- (18) Zhu, H., Contact Mechanism Based Asphalt Concrete Modeling, Proc. 12<sup>th</sup> ASCE Engineering Mechanics Conference, San Diego, May 1988.
- (19) Zhu, H. and J.E. Nodas, Contact Based Analysis of Asphalt Pavement with the Effect of Aggregate Angularity, Mech. Of Materials, Vol. 32, pp. 193-202, 2000.
- (20) Krishnan, J.M. and C.L. Rao, Mechanics of Air Voids Reduction of Asphalt Concrete Using Mixture Theory, Int. Jour. Eng. Sci., Vol. 38, pp. 1331-1354, 2000.
- (21) Rothenburg, L., Bogobowicz, A. and R. Haas, Micromechanical Modeling of Asphalt Concrete in Connection with Pavement Rutting Problems, Proc. 7<sup>th</sup> Intl. Conf. On Asphalt Pavements, Vol. 1, pp. 230-245, 1992.
- (22) Chang, G.K., and N.J. Meegoda, Simulation of the Behavior of Asphalt Concrete Using Discrete Element Method, Proc. 2<sup>nd</sup> Intl. Conf. On Discrete Element Methods, M.I.T, 1993.
- (23) Trent, B.C. and L.G. Margolin, Modeling Fracture in Cemented Granular Materials, ASCE Pub. Fracture Mechanics Applied to Geotechnical Engineering, Proc. ASCE National Convention, Atlanta, 1994.

- (24) Buttlar, W.G. and Z. You, Discrete Element Modeling of Asphalt Concrete: A Micro-Fabric Approach, Proc. 80<sup>th</sup> Transportation Research Board Meeting, Washington, D.C., 2001.
- (25) Ullidtz, P., A Study of Failure in Cohesive Particulate Media Using the Discrete Element Method, Proc. 80<sup>th</sup> Transportation Research Board Meeting, Washington, D.C., 2001.
- (26) Sadd, M.H. and J.Y. Gao, The Effect of Particle Damage on Wave Propagation in Granular Materials, *Mechanics of Deformation and Flow of Particulate Materials*, pp 159-173, Ed. C.S. Chang, A. Misra, R.Y. Liang and M. Babic, Proc. McNu Conference, Trans. ASCE, Northwestern Univ., June 1997.
- (27) Sadd, M.H., and J.Y. Gao, Contact Micromechanics Modeling of the Acoustic Behavior of Cemented Particulate Marine Sediments, Proc. 12th ASCE Engineering Mechanics Conf., La Jolla, CA, 1998.
- (28) Stankowski, T., Numerical Simulation of Progressive Failure in Particle Composites”, Ph.D. Thesis, University of Colorado, 1990.
- (29) Sepehr, K., O.J. Harvey, Z.Q. Yue and H.M. El Husswin, Finite Element Modeling of Asphalt Concrete Microstructure, Proc. 3<sup>rd</sup> Intl. Conf. Computer-Aided Assessment and Control Localized Damage, Udine, Italy, 1994.
- (30) Bazant, Z.P., Tabbara, M.R, Kazemi, T., and G. Pijaudier-Cabot, Random Particle Simulation of Damage and Fracture in Particulate or Fiber-Reinforced Composites, *Damage Mechanics in Engineering Materials*, AMD Vol 109, Trans. ASME, 1990.
- (31) Mora, P., A Lattice Solid Model for Rock Rheology and Tectonics, The Seismic Simulation Project Tech. Rep., Vol. 4, pp. 3-28, Institut de Physique du Globe, Paris, 1992.
- (32) Sadd, M.H., Qiu, L., Boardman, W., and A. Shukla, Modeling Wave Propagation in Granular Materials Using Elastic Networks”, *Intl. J. Rock Mechanics & Mining Sci*, Vol. 29, p. 61, 1992.

- (33) Budhu, M., Ramakrishnan, S. and G. Frantziskonis, Modeling of Granular Materials: A Numerical Model Using Lattices”, *Mechanics of Deformation and Flow of Particulate Materials*, Ed. C.S. Chang, A. Misra, R.Y. Liang and M. Babic, Proc. McNu Conference, Trans. ASCE, Northwestern Univ., June 1997.
- (34) Guddati, M.N., Z. Feng and Y.R. Kim, Towards a Micromechanics-Based Procedure to Characterize Fatigue Performance of Asphalt Concrete, Proc. 81<sup>st</sup> Transportation Research Board Annual Meeting, Washington, D.C., 2002.
- (35) Bahia, H., H. Zhai, K. Bonnetti and S. Kose, Nonlinear Viscoelastic and Fatigue Properties of Asphalt Binders, *J. Assoc. Asphalt Paving Tech.*, Vol. 68, pp. 1-34, 1999.
- (36) Papagiannakis, A.T., A. Abbas and E. Masad, Micromechanical Analysis of the Viscoelastic Properties of Asphalt Concretes, Proc. 81<sup>st</sup> Transportation Research Board Annual Meeting, Washington, D.C., 2002.
- (37) Mustoe, G.G.W. and D.V. Griffiths, An Equivalent Model Using Discrete Element Method (DEM), Proc. 12th ASCE Engineering Mechanics Conf., La Jolla, CA, 1998.
- (38) Sadd, M.H. and Q. Dai, Effect of Microstructure on the Static and Dynamic Behavior of Recycled Asphalt Material, University of Rhode Island Transportation Center Report # 536108, 2001.
- (39) Sadd, M.H., Shukla, A., Dai, Q. and V. Parameswaran, Mechanical Behavior of Recycled Asphalt Materials: Experimental and Theoretical Modeling Results, Proc. Intl. Conf. Of Beneficial Use of Recycled Materials in Transportation Applications, Arlington, VA, 2001.
- (40) Sadd, M.H., Dai, Q., Shukla, A. and V. Parameswaran, Microstructural Simulation of Asphalt Materials: Modeling and Experimental Verification, Proc. 15<sup>th</sup> Engineering Mechanics Conf., Columbia Univ., New York, NY, 2002.

- (41) Kennedy, T.W., Roberts, F.L. and K.W. Lee, Evaluation of Moisture Susceptibility of Asphalt Mixtures using Texas Freeze-Thaw Pedestal Test, Proc. of the Association of Asphalt Paving Technologists, Vol. 51, pp. 327-341, Kansas City, MO, 1982.
- (42) Zhong, X. and C.S. Chang, Micromechanical Modeling for Behavior of Cementitious Granular Materials, J. Eng. Mechanics, ASCE, Vol. 125, pp. 1280-1285, 1999.
- (43) Ishikawa, M., Yoshikawa, H. and T. Tanabe, The Constitutive Model in Terms of Damage Tensor, Proc. Of Finite Element Analysis of Reinforced Concrete Structures, ASCE Publication, Tokyo, pp. 93-103, 1986.